A&A 679, A69 (2023)
https://doi.org/10.1051/0004-6361/202347129

Astronomy & Astrophysics

Looking into the faintEst WIth MUSE (LEWIS): Exploring the nature of ultra-diffuse galaxies in the Hydra-I cluster

I. Project description and preliminary results

Enrichetta Iodice[1], Michael Hilker[2], Goran Doll[1,3], Marco Mirabile[4,5], Chiara Buttitta[1], Johanna Hartke[6,7], Steffen Mieske[8], Michele Cantiello[4], Giuseppe D'Ago[9], Duncan A. Forbes[10], Marco Gullieuszik[11], Marina Rejkuba[2], Marilena Spavone[1], Chiara Spiniello[12], Magda Arnaboldi[2], Enrico M. Corsini[11,13], Laura Greggio[11], Jesus Falcón-Barroso[14], Katja Fahrion[15], Jacopo Fritz[16], Antonio La Marca[17,18], Maurizio Paolillo[1,3], Maria Angela Raj[17], Roberto Rampazzo[11], Marc Sarzi[19], and Giulio Capasso[1]

(Affiliations can be found after the references)

Received 8 June 2023 / Accepted 10 August 2023

ABSTRACT

Looking into the faintEst WIth MUSE (LEWIS) is an ESO large observing programme that aims at obtaining the first homogeneous integral-field spectroscopic survey of 30 extremely low-surface-brightness (LSB) galaxies in the Hydra I cluster of galaxies with MUSE at ESO-VLT. The majority of LSB galaxies in the sample (22 in total) are ultra-diffuse galaxies (UDGs). Data acquisition started in December 2021 and is expected to be concluded by March 2024. Up to June 2023, 29 targets were observed and the redshift has been derived for 20 of them. The distribution of systemic velocities $V_{\rm sys}$ ranges between 2317 km s^{-1} and 5198 km s^{-1} and is centred on the mean velocity of Hydra I ($V_{\rm sys}$ = 3683 ± 46 km s^{-1}). Considering the mean velocity and the velocity dispersion of the cluster ($\sigma_{\rm cluster} \sim 700$ km s^{-1}), 17 out of 20 targets are confirmed cluster members. The three objects with velocities of greater than $2\sigma_{\rm cluster}$ away from the cluster mean velocity could be two background galaxies and one foreground galaxy. To assess the quality of the data and demonstrate the feasibility of the science goals, we report the preliminary results obtained for one of the sample galaxies, UDG11. For this target, we *(i)* derived the stellar kinematics, including the two-dimensional maps of line-of-sight velocity and velocity dispersion, *(ii)* constrained age and metallicity, and *(iii)* studied the globular cluster (GC) population hosted by the UDG. Results are compared with the available measurements for UDGs and dwarf galaxies in the literature. By fitting the stacked spectrum inside one effective radius, we find that UDG11 has a velocity dispersion of $\sigma = 20 \pm 8$ km s^{-1} and is old (10 ± 1 Gyr), metal-poor ([M/H] = −1.17 ± 0.11 dex), and has a total dynamical mass-to-light ratio of $M/L_V \sim 14$, which is comparable to those observed for classical dwarf galaxies. The spatially resolved stellar kinematics maps suggest that UDG11 does not show a significant velocity gradient along either its major or minor photometric axis, and the average value of the velocity dispersion is $\langle\sigma\rangle_{\rm e} = 27 \pm 8$ km s^{-1}. We find two GCs kinematically associated with UDG11. The estimated total number of GCs in UDG11 – corrected for the spectroscopic completeness limit – is $N_{\rm GC} = 5.9^{+2.2}_{-1.8}$, which corresponds to a GC-specific frequency of $S_N = 8.4^{+3.2}_{-2.7}$.

Key words. galaxies: clusters: individual: Hydra I – galaxies: dwarf – galaxies: kinematics and dynamics – galaxies: stellar content – galaxies: formation

1. Introduction

Ultra-diffuse galaxies (UDGs) are among the faintest and lowest-surface-brightness ($\mu_{0,g} \geq 24$ mag arcsec^{-2}, $R_{\rm e} \geq 1.5$ kpc) galaxies known in the Universe. Very low-surface-brightness (LSB) galaxies were first recognised in the 80s; they were discovered in the Virgo and Fornax clusters decades ago (Sandage & Binggeli 1984; Impey et al. 1988; Ferguson & Sandage 1988; Bothun et al. 1991). The term UDG was introduced by van Dokkum et al. (2015), who detected several galaxies, including an extremely faint and diffuse galaxy named DF44 in the Coma cluster with an effective radius of $R_{\rm e} \sim 4.3$ kpc, similar to that of the Milky Way ($R_{\rm e} \sim 4.5$ kpc), but with a 100 times smaller stellar mass.

Being so diffuse and faint, in order to survive cluster tides UDGs should host a large amount of dark matter (van Dokkum et al. 2015). This idea has brought ever-increasing attention to the detection and study of UDGs and has given these galaxies a special role in the realm of the LSB Universe. Given the extremely low baryonic mass density, UDGs are indeed considered particularly suitable laboratories for testing the formation of galaxies in the Λ-cold dark matter (ΛCDM) framework.

Since 2015, several observational campaigns have been carried out in order to obtain deep images mapping different environments from groups to clusters of galaxies, and these have provided large samples of LSB galaxies, including UDGs (Yagi et al. 2016; van der Burg et al. 2017; Trujillo et al. 2017; Venhola et al. 2017; Janssens et al. 2019; Mancera Piña et al. 2019; Prole et al. 2019a; Román et al. 2019; Lim et al. 2020; Marleau et al. 2021; La Marca et al. 2022a; Zaritsky et al. 2022). To classify an LSB galaxy as a UDG, the most conservative approach is based on the empirical definition proposed by van Dokkum et al. (2015). This requires UDGs to have a central surface brightness fainter than 24 mag arcsec^{-2} (in the g band) and an effective radius of greater than 1.5 kpc. However, other criteria have also been proposed that use different cuts in size and/or surface-brightness limit (Koda et al. 2015; Yagi et al. 2016; van der Burg et al. 2017; Mancera Piña et al. 2019). In particular, taking advantage of a large and statistically significant sample of dwarf and LSB galaxies in the Virgo

cluster, Lim et al. (2020) found that UDGs can be classified as the extremes in the broad scaling relationships between photometric and structural properties of LSB galaxies (e.g. total luminosity vs. R_e and μ_e). UDGs have been found to be $\sim 2.5\sigma$ fainter and larger than the average distribution of the parent dwarf galaxy sample. These results support the idea that UDGs can be considered as extreme LSB tail of the size–luminosity distribution of dwarf galaxies.

The considerable amount of imaging data collected to date for UDGs has shown that these galaxies span a wide range of structural and photometric properties. Based on their integrated colours, it seems that two populations of UDGs exist: red UDGs are mainly found in clusters of galaxies, while bluer objects are discovered in the low-density regions, that is, in the outskirts of clusters and in the field (see e.g. Román & Trujillo 2017; Leisman et al. 2017; Prole et al. 2019b; Marleau et al. 2021). Red UDGs are also found in groups of galaxies (Marleau et al. 2021).

Deep images have also allowed the detection and study of globular cluster (GC) populations in UDGs. By deriving the GC-specific frequency ($S_N = N_{GC} \times 10^{0.4(M_V+15)}$, Harris & van den Bergh 1981), observations from space- and ground-based telescopes have revealed an extreme degree of variability in S_N values. Some UDGs are consistent with having no GC population, while others present an S_N as high as ∼150 (Prole et al. 2019a; Saifollahi et al. 2021, 2022; Marleau et al. 2021; La Marca et al. 2022a). The unusually high S_N in some UDGs triggered a debate about the fraction of DM in UDGs. Assuming that the relation between the total number of GCs, N_{GC}, and the host galaxy's halo virial mass – which is valid from giant to dwarf galaxies (see Burkert & Forbes 2020, and references therein) – also holds in the LSB regime, UDGs with large N_{GC} values might be DM-dominated systems with 100 times more massive halo masses ($M_h \geq 10^{11}\ M_\odot$) than higher-surface-brightness dwarf galaxies of similar luminosity.

To date, the DM content of the UDGs is a highly debated topic. The few spectroscopic studies, which focus on special cases, point to a rather diverse population. Some UDGs were found to host a very massive DM halo (Toloba et al. 2018; van Dokkum et al. 2019; Forbes et al. 2021; Gannon et al. 2021), while at the same time there are some UDGs with a 'normal' DM halo; that is, they have a DM content that is consistent with that of other dwarf galaxies of similar luminosity. Finally, a few UDGs have also been found to populate the opposite extreme, and are said to be almost DM-free (van Dokkum et al. 2018; Collins et al. 2021).

Because of their LSB nature, getting spectroscopic data for UDGs is a challenging task. To date, as opposed to the availability of deep images, we still lack a statistically significant sample of UDGs with spectroscopy, which strongly limits our constraints and conclusions on their stellar populations and DM content. For two to three dozen UDGs, the available spectroscopic studies reveal the existence of both metal-poor ($-0.5 \leq [M/H] \leq -1.5$ dex) and old systems (∼9 Gyr; e.g. Ferré-Mateu et al. 2018; Pandya et al. 2018; Fensch et al. 2019), as well as younger star-forming UDGs (Martín-Navarro et al. 2019). The kinematic measurements of UDGs available in groups and clusters suggest that the rotation velocity of the stars is very low (see Gannon et al. 2023, and references therein).

The wide range of photometric and spectroscopic properties, including the content of GCs, does not fit into a single formation scenario, and there is a general consensus that different formation channels can be invoked to form galaxies with UDG-like properties. van Dokkum et al. (2015) coined the term 'failed' galaxies, suggesting that these objects with high DM content and large effective radii might have lost their gas supply at an early epoch, evolving to become quenched and diffuse galaxies. Since then, a plethora of UDG formation mechanisms have been proposed that are nicely able to form a galaxy with the typical morphology of UDGs, but these predict different DM amounts, ages, metallicities, and gas content. The formation scenarios most consistent with the observational properties of UDGs have been identified.

For simplicity, formation scenarios for UDGs can be divided into two groups based on the physical processes at work: internal and external mechanisms. Star-formation feedback and highly rotating DM halos are both possible internal mechanisms that can form large and diffuse galaxies. In the former case, repeated star formation episodes during early galaxy evolution can drive the gas out to large radii and prevent subsequent star formation (Di Cintio et al. 2017). In the latter case, the high specific angular momentum of a DM halo prevents gas from effectively collapsing into a dense structure (Amorisco & Loeb 2016; Rong et al. 2017; Tremmel et al. 2019). In both scenarios, the resulting UDGs are gas-rich and have a 'normal', dwarf-like DM halo.

Gravitational interactions and merging between galaxies, as well as interactions with the environment, are external processes that might shape galaxies to become UDG-like. Similar to the tidal dwarf galaxies (TDGs), UDGs might originate from the collisional debris of a merger (Lelli et al. 2015; Duc et al. 2014; Ploeckinger et al. 2018). Poggianti et al. (2019) suggested that UDGs might form from ram-pressure-stripped gas clumps in the extended tails of infalling cluster galaxies. Both scenarios predict blue, dusty, star-forming, and DM-free UDGs, with moderate to low metallicity and UV emission. Weak tidal interaction of a dwarf galaxy with a massive nearby giant galaxy has also been addressed as a possible UDG formation mechanism (Conselice 2018; Carleton et al. 2021; Bennet et al. 2018; Müller et al. 2019; Gannon et al. 2021). High-velocity galaxy collisions might generate several debris, with some of them could remain gravitationally bound systems with a UDG-like structure (Silk 2019; Shin et al. 2020; van Dokkum et al. 2022). Also in these latter cases, the formed UDGs are expected to be DM-free galaxies, but red and gas-poor. UDGs could also form from large dwarf galaxies, which, during their interaction with the cluster environment, had their gas removed by ram-pressure stripping, halting subsequent star formation (Yozin & Bekki 2015; Tremmel et al. 2020). The resulting UDG is gas poor and has a dwarf-like DM content. Finally, in the framework of external processes, a quenched, isolated, gas-poor UDG with a dwarf-like DM halo might end up as a backsplash galaxy. In this case, former satellites of a group or cluster halo in an early epoch are now found a few megaparsecs away from the group or cluster (Benavides et al. 2021). All of the above scenarios and related predicted properties for UDGs are summarised in Fig. 1.

Based on the IllustrisTNG simulations, Sales et al. (2020) proposed two different formation channels for cluster UDGs. A population of 'born UDGs' (B-UDGs) could form in the field and later enter the cluster environment. The B-UDGs originate from LSB galaxies that, having joined the cluster potential, lost their gas supply and were quenched. Differently, tidal forces could act on luminous galaxies in the cluster, removing their DM and puffing up their stellar component. As a consequence, these galaxies evolve into UDGs, and are named 'tidal-UDGs' (T-UDGs). T-UDGs populate the centre of the clusters and, at a given stellar mass, have lower velocity dispersion, higher metallicity, and lower DM fraction with respect to the B-UDGs.

In summary, observations strongly suggest that the class of UDGs might comprise different types of galaxies, with different intrinsic properties (e.g. colours, stellar populations, and DM fractions). Theoretical works on UDGs, also reviewed above, show that more than one formation channel might exist to account for the different types of UDGs, or, reasonably, a combination of physical processes may account for environmental effects. The lack of stellar kinematics and stellar population properties is the main limitation to providing stringent conclusions as to the nature of UDGs and to discriminating between the formation channels.

In this paper, we present the 'Looking into the faintEst WIth MUSE' (LEWIS) project, aims at obtaining the first homogeneous integral-field spectroscopic survey of 30 extreme LSB galaxies – including UDGs – in the Hydra I cluster of galaxies with MUSE at ESO-VLT. Doubling the number of spectroscopically studied UDGs, with this project we will make a decisive impact in this field. With LEWIS we will map, for the first time, the stellar population and DM content of a complete sample of UDGs in a galaxy cluster based on spectroscopic data.

The present paper is organised as follows. The galaxy sample and science goals of the LEWIS project are presented in Sect. 2. Observations and data reduction are described in Sect. 3. The redshift estimates for all of the UDGs observed so far are provided in Sect. 4. In Sect. 5, we present our analysis of the MUSE data, with a detailed description for one of the galaxies in the sample, UDG11, which was chosen as a test case. The preliminary results are discussed in Sect. 6, and conclusions are provided in Sect. 7.

2. Galaxy sample and science goals of the LEWIS project

LEWIS is an ESO Large Programme that began in 2021, and was approved during the ESO period 108 (P.I. E. Iodice, ESO programme ID 108.222P). The aim of LEWIS is to obtain the first homogeneous integral-field spectroscopic survey of UDGs in the Hydra I cluster of galaxies (see Fig. 2). This is a rich environment of galaxies located in the southern hemisphere at a distance of 51 ± 6 Mpc (Christlein & Zabludoff 2003), with a virial mass of $2 \times 10^{14}\,M_{\odot}$ (Girardi et al. 1998), a virial radius of $R_{\rm vir} \sim 1.6$ Mpc, and a velocity dispersion of $\sigma_{\rm cluster} \simeq 700\,{\rm km\,s^{-1}}$ (Lima-Dias et al. 2021). Hydra I has been extensively studied using deep images and multi-object spectroscopy (e.g. Misgeld et al. 2008, 2011; Richtler et al. 2011; Arnaboldi et al. 2012; Hilker et al. 2018; Barbosa et al. 2018, 2021). Results from the literature show that this cluster is still in an active phase of mass assembly, because ongoing interactions are detected around the brightest cluster member NGC 3311 (see Barbosa et al. 2018; Iodice et al. 2021, and references therein). The projected distribution of all cluster members, that is, bright galaxies and dwarfs, shows three main over-densities: the core of the cluster, around NGC 3311 and NGC 3309, a subgroup of galaxies elongated north–south, and a subgroup of galaxies in the southeast region of the cluster (La Marca et al. 2022a).

The latest Hydra I catalogue presents 317 galaxies fainter than $M_r > -18.5$ mag and a semi-major axis of greater than 200 pc, of which about 230 new candidates were recently discovered by Iodice et al. (2020, 2021) and La Marca et al. (2022a,b). The authors studied the photometric properties of this class of objects; these are briefly summarised below. According to the colour–magnitude relation for early-type giant and dwarf galaxies in Hydra I (Misgeld et al. 2008), all of the new candidates are consistent with being cluster members. In this sample, according to the definition proposed by van Dokkum et al. (2015), that is, $R_{\rm e} \geq 1.5$ kpc and $\mu_{0,g} \geq 24\,{\rm mag\,arcsec^{-2}}$, 22 objects are classified as UDGs (Iodice et al. 2020, 2021; La Marca et al. 2022a). An additional 10 galaxies, which are very extended ($R_{\rm e} \geq 1.5$ kpc) but with $\mu_{0,g} \geq 23\,{\rm mag\,arcsec^{-2}}$, were classified as LSB dwarfs. Taking into account the virial mass of $\sim 10^{14}\,M_{\odot}$ for the Hydra I cluster (see Fig. 6 in La Marca et al. 2022a), and the UDG abundance-halo mass relation ($N_{\rm UDG} \propto M_{200}^{1.11}$; van der Burg et al. 2017), the expected number of UDGs in Hydra I within $1R_{\rm vir}$ is 48 ± 10 UDGs. Therefore, the detection of 22 UDGs inside $\simeq 0.4R_{\rm vir}$ of the Hydra I cluster can be considered a complete sample for this class of objects. Based on photometric and size selection, GC candidates are identified around a few of those LSB galaxies, with a total number of GCs per galaxy of $N_{\rm GC} \geq 2$.

The newly discovered LSB dwarfs and UDGs span a wide range of central surface brightness ($23 \leq \mu_{0,g} \leq 27\,{\rm mag\,arcsec^{-2}}$) and effective radius ($1 \leq R_{\rm e} \leq 4$ kpc). Compared to the population of early-type dwarf galaxies in the cluster, they have similar integrated $g-r$ colours, $0.4 \leq g-r \leq 0.9$ mag, and stellar masses of $M_{\star} = 5 \times 10^6 - 2 \times 10^8\,M_{\odot}$. Inside $\simeq 0.4R_{\rm vir}$ of the Hydra I cluster, the structural and photometric parameters (i.e. surface brightness, size, colour, and Sersic n-index) and GC content of all LSB galaxies have similar properties and trends to those observed for dwarf galaxies. Therefore, as addressed by La Marca et al. (2022a), these findings suggest that a single population of LSB galaxies is present in this region of the cluster, and UDGs can be reasonably considered as the extreme LSB tail of the size-luminosity distribution of all dwarfs in this environment. Finally, the LSB galaxies share a similar 2D projected distribution to that observed for the dwarf and giant galaxies in the cluster: over-densities are found in the cluster core and north of the cluster centre. Similar results are found for other galaxy clusters, where over-densities of UDGs are observed close to subgroups of other cluster members (see e.g. Janssens et al. 2019). The observation of UDGs spatially associated with groups infalling onto the cluster would further support the idea that they might follow two formation paths, as proposed by Sales et al. (2020). In summary, the previous results and ongoing studies on UDGs in Hydra I suggest that this environment offers a unique opportunity to analyse this class of LSB galaxies in great detail.

The nature and formation of UDGs can be explored by measuring their kinematics, stellar population, and DM content as a function of their location in the cluster. The here-to best-studied environment where UDGs have been investigated, Hydra I, is at half the distance of the Coma cluster and is ten times less massive. Therefore, Hydra I offers an exquisite opportunity to analyse LSB galaxies – including UDGs – in an environment of different mass scales, and to relate their properties to the mass assembly processes. In particular, if the new spectroscopic data from the LEWIS project confirm the asymmetric distribution of UDGs, we can investigate whether the galaxies in the subgroups have different properties from those in the outskirts of the cluster, indicating that the latter systems formed as genuine UDGs, and are different from those in the denser inner environment.

Given the large variety of observed properties (mainly based on deep images) and theoretical predictions, the LEWIS project will provide a notable boost to our knowledge of UDG structure and formation in a cluster environment (see Forbes et al. 2023). In particular, we expect to address the following science goals, which refer to the main debated issues on the nature of UDGs:

– DM content of each UDG of the sample through dynamical mass estimates from stellar kinematics. As the UDGs are not

Formation channel	Expected properties
failed ($M_* \sim 10^{11}$ $M_\odot$) galaxies (van Dokkum et al. 2015)	red, quenched, metal poor & old, gas poor, DM dominated
Internal processes	
star-formation feedback (Di Cintio et al. 2017)	gas rich, dwarf-like DM halo
high-spin DM halo (Amorisco & Loeb 2016; Rong et al. 2017; Tremmel et al. 2019)	gas rich, dwarf-like DM halo
External mechanisms	
gravitational interactions & merging - ***collisional debris of a merger, i.e. TDG-like*** (Lelli et al. 2015; Duc et al. 2014; Ploeckinger et al. 2018) - ***ram-pressure stripped clumps*** (Poggianti et al. 2019)	blue, dust, moderate metallicity, SF, UV emission & gas rich, DM-free
gravitational interactions & merging - ***weak tidal interaction*** (Conselice 2018; Carleton et al. 2021; Bennet et al. 2018; Müller et al. 2019) - ***high-velocity galaxy collisions*** (Silk 2019; Shin et al. 2020; van Dokkum et al. 2022)	red, metal poor, gas free, DM free
interaction with the environment (Yozin & Bekki 2015; Tremmel et al. 2020)	gas poor dwarf-like DM halo
backsplash galaxies (Benavides et al. 2021)	quenched, isolated, gas poor, dwarf-like DM halo, near to a high density environment

Fig. 1. Schematic view of the main formation channels proposed for UDGs. The left boxes list the relevant physical processes. The predicted properties of UDGs from each of the formation channels are reported in the boxes on the right.

uniformly distributed inside the cluster, we will check whether or not the DM content correlates with the environment in which the UDG resides.

– Star formation history of UDGs from SED fitting of their integrated spectra. This allows us to study the evolutionary link between the UDGs and other dwarf galaxies through a comparison of their stellar population and structural properties.

– Spectroscopic confirmation of GC candidates around UDGs, which will improve their S_N estimates, and in turn will provide a firmer basis to the discussion of the possible overdensities of GCs around some UDGs and the relation to the host-galaxy DM content.

To these aims, the main objectives of LEWIS are to derive the stellar kinematics, stellar populations, and the spectroscopic specific frequency S_N of the hosted GCs for all the selected galaxies in our sample. As stated in Sect. 1, similar studies are available for only about 35 UDGs in total, mainly in the Coma cluster (van Dokkum et al. 2017; Ruiz-Lara et al. 2018; Ferré-Mateu et al. 2018; Gu et al. 2018). In particular, integral-field (IF) spectroscopy is available for only about a dozen UDGs (Martín-Navarro et al. 2019; Emsellem et al. 2019; Müller et al. 2020; Gannon et al. 2021, 2023; Webb et al. 2022).

From the sample of 32 LSB galaxies photometrically detected in the Hydra I cluster (Iodice et al. 2020; La Marca et al. 2022a), we selected 30 objects (22 UDGs and 8 LSB galaxies) for the spectroscopic follow-up with MUSE at ESO-VLT within our LEWIS project. They were selected to have an effective surface brightness in the range $25 \leq \mu_e \leq 27.5$ mag arcsec^{-2} in the g band, which provides the minimum signal-to-noise ratio ($S/N \sim$ 5–10, depending on the surface brightness) per spaxel in a reasonable integration time (~2–6 h), which is required for the main goals of this project. The two targets excluded from the spectroscopic LEWIS follow-up, UDG14 and UDG19 in La Marca et al. (2022a), are the faintest objects of the photometric sample, with $\mu_e = 28.5$ mag arcsec^{-2} in the g band. According to the colour–magnitude relation (see Fig. 3 in La Marca et al. 2022a), both galaxies can be considered as Hydra I cluster members. Galaxies in the LEWIS sample are listed in Table 1 and shown in Fig. 2.

3. Observations and data reduction

The LEWIS observations are carried out with the MUSE integral-field spectrograph mounted on the Yepun Unit Telescope 4 at the ESO Very Large Telescope in Chile. MUSE is used in Wide Field Mode without adaptive optics, providing a field of view (FoV) of 1×1 arcmin^2, with a spatial sampling of 0.2×0.2 arcsec^2. The nominal wavelength range of MUSE is from 4800 to 9300 Å with a spectral resolution (FWHM) that varies from 2.74 Å (69 km s^{-1}) at 5000 Å to 2.54 Å (46 km s^{-1}) at 7000 Å (Bacon et al. 2017).

Table 1. LEWIS sample: UDG and LSB galaxies in the Hydra I cluster.

Object	RA	Dec	M_r	M_*	μ_e	μ_0	R_e	N_{GC}	Obs. status	Exp. time	V_{sys}
	[J2000]	[J2000]	[mag]	[$10^8\,M_\odot$]	[mag arcsec^{-2}]	[mag arcsec^{-2}]	[kpc]			[h]	[km s^{-1}]
(1)	(2)	(3)	(4)	(5)	(6)	(7)	(8)	(9)	(10)	(11)	(12)
UDG 1	10:37:54.12	−27:09:37.50	−15.48	1.12	25.2 ± 0.1	24.2 ± 0.1	1.75 ± 0.12	0 ± 1	C	2.00	4219 ± 9
UDG 2	10:37:34.89	−27:10:29.94	−14.27	0.55	26.2 ± 0.1	25.0 ± 0.1	1.55 ± 0.12	7 ± 3	P	1.33	–
UDG 3	10:36:58.63	−27:08:10.21	−14.70	1.65	26.1 ± 0.2	25.2 ± 0.2	1.88 ± 0.12	15 ± 6	C	3.00	3550 ± 26
UDG 4	10:37:02.64	−27:12:15.01	−16.03	10.6	25.8 ± 0.1	24.9 ± 0.1	2.64 ± 0.12	2 ± 1	C	2.00	2317 ± 13
UDG 5	10:36:07.68	−27:19:03.26	−14.66	1.16	25.3 ± 0.3	23.7 ± 0.3	1.42 ± 0.12	0 ± 1	S	–	–
UDG 6	10:36:35.80	−27:19:36.12	−14.38	0.32	25.3 ± 0.1	24.1 ± 0.1	1.37 ± 0.12	0 ± 1	P	0.75	–
UDG 7	10:36:37.16	−27:22:54.93	−13.72	0.49	26.9 ± 0.4	24.4 ± 0.4	1.66 ± 0.12	3 ± 1	C	3.80	4134 ± 28
UDG 8	10:38:14.59	−27:24:27.07	−14.87	0.53	25.0 ± 0.6	23.2 ± 0.6	1.40 ± 0.12	0 ± 1	P	0.75	4793 ± 16
UDG 9	10:37:22.85	−27:36:02.80	−15.16	1.78	26.8 ± 0.2	24.2 ± 0.2	3.46 ± 0.12	7 ± 1	C	3.90	4302 ± 13
UDG 10	10:35:27.32	−27:33:03.86	−13.89	0.26	27.3 ± 0.3	24.3 ± 0.3	2.29 ± 0.10	0 ± 1	C	3.85	3577 ± 139
UDG 11	10:34:59.55	−27:25:37.95	−14.75	0.63	25.7 ± 0.1	24.4 ± 0.1	1.66 ± 0.12	7 ± 3	C	6.10	3507 ± 3
UDG 12	10:36:45.55	−27:48:12.73	−14.30	1.19	26.2 ± 0.2	25.1 ± 0.2	1.64 ± 0.12	0 ± 1	P	1.50	4615 ± 13
UDG 13	10:36:14.49	−27:30:26.60	−12.73	0.20	27.3 ± 0.1	24.2 ± 0.2	1.60 ± 0.20	–	C	3.93	3438 ± 52
UDG 15	10:36:02.55	−27:36:19.57	−11.95	0.06	27.7 ± 0.2	25.0 ± 0.3	1.51 ± 0.15	2 ± 3	C	4.68	3553 ± 88
UDG 16	10:36:25.30	−27:14:14.74	−12.84	0.11	27.6 ± 0.1	25.9 ± 0.2	1.75 ± 0.12	–	S	–	–
UDG 17	10:36:41.72	−27:16:37.48	−13.99	1.20	26.7 ± 0.1	24.9 ± 0.1	1.50 ± 0.20	3 ± 3	P	1.50	–
UDG 18	10:36:16.82	−27:20:16.84	−12.28	0.09	27.6 ± 0.2	25.6 ± 0.2	1.64 ± 0.12	11 ± 7	C	4.70	–
UDG 20	10:38:04.43	−27:29:50.18	−12.95	0.14	27.3 ± 0.1	26.0 ± 0.3	1.97 ± 0.12	–	C	3.88	4693 ± 12
UDG 21	10:36:54.17	−27:36:55.07	−12.78	0.11	27.3 ± 0.5	24.0 ± 0.4	1.50 ± 0.12	–	C	3.88	3489 ± 22
UDG 22	10:34:40.97	−27:42:03.27	−13.92	0.36	26.5 ± 0.1	25.3 ± 0.2	3.60 ± 0.12	–	P	1.50	5198 ± 5
UDG 23	10:35:27.70	−27:46:16.58	−14.11	0.34	27.2 ± 0.2	24.3 ± 0.3	2.47 ± 0.20	–	C	2.10	3496 ± 33
UDG 32	10:37:04.20	−27:42:53.92	−14.65	8.00	27.5 ± 1.0	26.2 ± 1.0	3.80 ± 1.00	7 ± 4	C	5.00	–
LSB 1	10:36:00.03	−27:28:58.17	−12.38	0.06	26.6 ± 0.1	23.9 ± 0.2	0.81 ± 0.90	–	S	–	–
LSB 2	10:36:09.65	−27:30:51.61	−12.87	0.15	25.8 ± 0.1	23.8 ± 0.1	0.57 ± 0.12	–	P	0.75	–
LSB 3	10:36:26.55	−27:32:41.61	−12.03	0.05	26.6 ± 0.8	23.7 ± 0.6	0.70 ± 0.12	–	S	–	–
LSB 4	10:36:19.71	−27:13:41.68	−13.83	0.25	26.5 ± 0.1	24.7 ± 0.1	1.48 ± 0.12	8 ± 3	C	3.00	3420 ± 44
LSB 5	10:36:41.26	−27:48:20.54	−13.74	0.40	25.8 ± 0.1	23.9 ± 0.1	1.42 ± 0.12	–	P	0.75	3439 ± 40
LSB 6	10:38:04.67	−27:32:44.99	−15.47	1.84	26.0 ± 0.1	23.0 ± 0.2	4.00 ± 1.00	2 ± 1	C	2.30	5193 ± 5
LSB 7	10:36:18.70	−27:37:17.93	−15.68	2.59	25.3 ± 0.1	22.7 ± 0.1	1.97 ± 0.10	–	P	0.75	3551 ± 11
LSB 8	10:37:54.47	−27:15:31.12	−15.27	1.44	25.1 ± 0.1	23.2 ± 0.2	1.51 ± 0.20	–	P	0.75	2718 ± 5

Notes. Column 1 reports the name of the target in the LEWIS sample. Columns 2 and 3 list the coordinates. Columns 4 and 5 report the total r-band magnitude and stellar mass, respectively, derived from the r-band image. Columns 6–8 list the structural parameters in the g band published by Iodice et al. (2020) and La Marca et al. (2022a): effective surface brightness, central surface brightness, and effective radius in kpc, respectively. Magnitudes and colours are corrected for Galactic extinction using values from Schlegel et al. (1998). Column 9 reports the total number of GCs, which is statistically estimated from photometric data within $1.5R_e$ and corrected for photometric and spatial incompleteness (Iodice et al. 2020; La Marca et al. 2022a). Column 10 reports the status of the data acquisition until May 2023: C for completed, P for partially completed, and S for scheduled. The total integration time in hours is listed in Col. 11. Missing values are for those targets that are either not fully observed yet or are pending final analysis. Their velocities will be reported in a future paper. In Col. 12 we report the systemic velocity derived in this work. Missing values are for those targets that have not yet been observed.

Observations started in December 2021 during ESO period P108, and continued in periods P109 and P110. They are acquired in service mode under dark and clear conditions. In the first two observing periods (P108 and P109), we gave priority to those UDGs that are fully consistent with the empirical classification proposed by van Dokkum et al. (2015), i.e. $R_e \geq 1.5$ kpc and $\mu_{0,g} \geq 24$ mag arcsec^{-2}, and having photometrically detected GC candidates. Observations scheduled in P108 and P109 have been completed. The data acquisition for P110 targets – which are mostly LSB galaxies not classified as UDGs – is ongoing, with a completion of ∼20% in May 2023. In each run, and for each target, observations are executed in two steps. Shallower data are acquired to confirm the redshift first, and then, for the confirmed cluster members, we obtained longer exposures to reach the depth required for our scientific purposes.

As galaxies in the LEWIS sample span a wide range of effective surface brightness $25 \leq \mu_e \leq 27$ mag arcsec^{-2}, the total integration time adopted for each target was set by a required limiting magnitude $\mu_{lim} = \mu_e$ and a minimum $S/N = 7$ in a spectral bin (=2.51 Å) of 2×2 pixels for the brighter targets and 5×5 pixels for the fainter targets. Given that, the total integration times range from 2 h for galaxies with $\mu_e \simeq 25$ mag arcsec^{-2} up to ∼6 h for targets with $\mu_e \simeq 27$ mag arcsec^{-2}. The total integration time for each target and the status of the data acquisition are reported in Table 1. We applied a dither of 0.3–1.3 arcsec and a rotation by 90° between single exposures in order to minimise the signature of the 24 MUSE slices on the field of view.

3.1. Data reduction

Data are initially reduced with the MUSE pipeline version 2.8.5 (Weilbacher et al. 2016, 2020) within the ESOREFLEX environment (Freudling et al. 2013). The main steps include bias and overscan subtraction, flat-fielding correction, wavelength calibration, determination of the line spread function, and illumination correction. As all LEWIS targets are less extended than the MUSE FoV (see also Fig. 3), the sky has been evaluated directly on the science frames, as described in the following section. The flux calibration was obtained using spectro-photometric standard stars observed as part of the

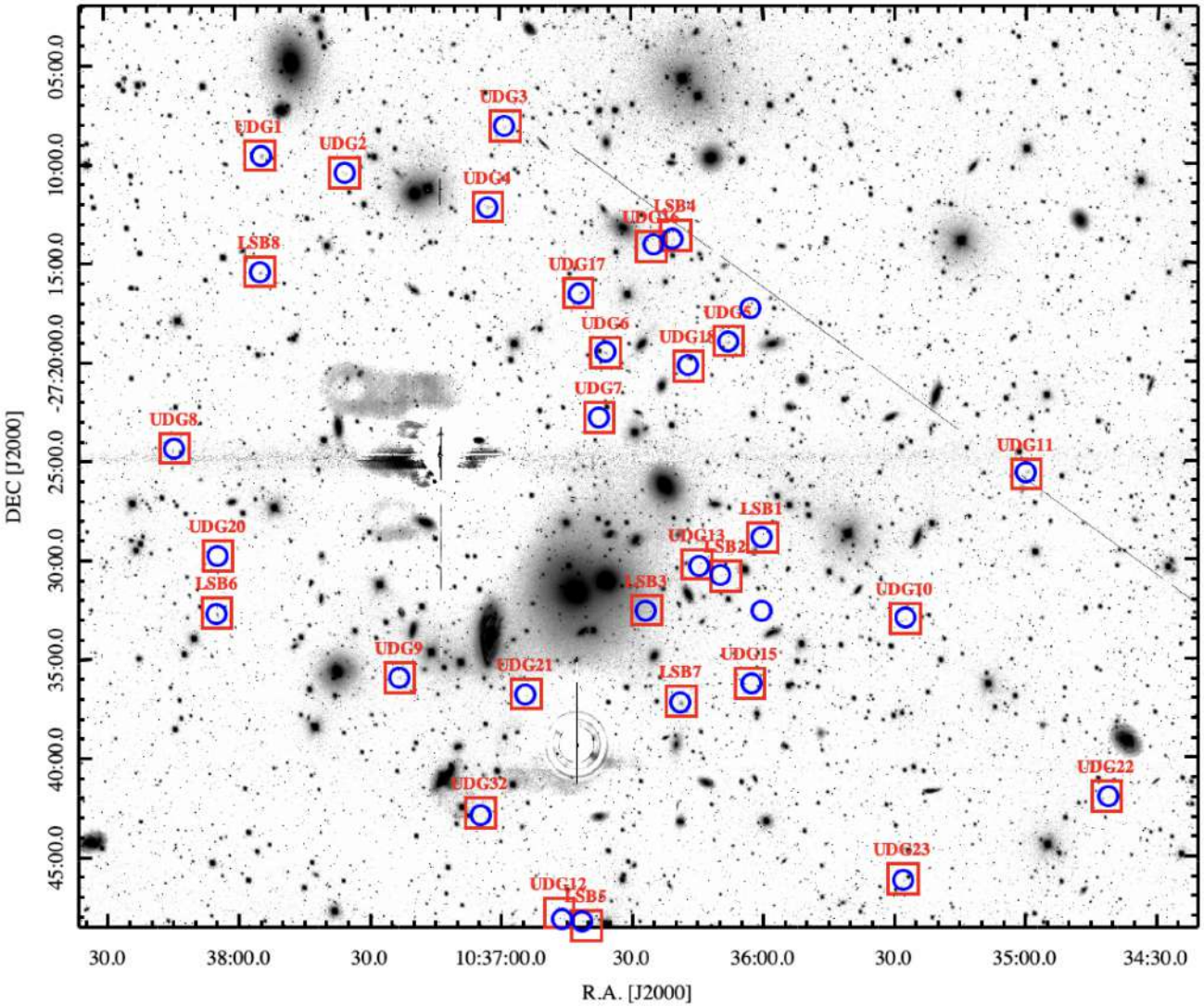

Fig. 2. Optical g-band mosaic from VST of the Hydra I cluster ($56.7' \times 46.55' \sim 0.8 \times 0.7$ Mpc). North is up and East to the left. The two bright stars, close to the cluster core, where modelled and subtracted from the image, as explained in Iodice et al. (2020). The 32 new UDGs and LSB galaxies detected by Iodice et al. (2020) and La Marca et al. (2022a) are marked as blue circles. Red boxes show the LEWIS sample presented in this work and listed in Table 1.

MUSE calibration plan. For each galaxy of the sample, the single exposures were aligned using reference stars and then combined to produce a first version of a stacked MUSE cube. In this first pipeline reduction, some of the default pipeline parameters for the sky subtraction and alignment for stacking were optimised[1].

3.2. Sky subtraction

After running the standard MUSE data reduction workflow, we used the resulting data products to obtain the final data cube with an improved sky subtraction, adapting the workflow described in Zoutendijk et al. (2020). The method and tools described below have been applied to one UDG of the sample, UDG11, chosen as a test case (see also Sect. 5). We used the reconstructed r-band image from the first version of the stacked MUSE cube to create an object mask. Objects were detected on the background-subtracted and Gaussian kernel convolved r-band image with the `photutils` software (Bradley et al. 2020). The resulting object mask was dilated by a factor of two and covers all visually detected foreground and background objects in the r-band image. To also cover the faint outskirts of the UDG that remained unmasked by the automatic object detection, we manually added an ellipse covering the central $1R_e$ of UDG 11 ($R_e = 1.66$ kpc, ellipticity $\epsilon = 0.3$, position angle P.A. = 144°; Iodice et al. 2020).

We then ran ESOREFLEX again with the following modifications to the standard workflow. As we now used custom sky masks, we increased the fraction of pixels considered as the sky to `SkyFr_2=0.75`. Masking any non-sky objects in the sky also allowed us to use the autocalibration routines and we thus set `autocalib=deepfield`. The autocalibration method was originally developed for the MUSE deep field and uses the sky background to estimate correction factors for each slice in several wavelength bins after the rejection of outliers (Weilbacher et al. 2020), removing the spatial structure from MUSE exposures that remained after flat fielding. We also applied multiplicative flux calibration to each exposure before exposure combination,

[1] Sky subtraction: `SkyMethod=auto`, `skymodel_ignore=0.02`, `SkyFr_2=0.1`; Source alignment: `threshold=8`, `bkgfraction=0.2`, `srcmin=8`.

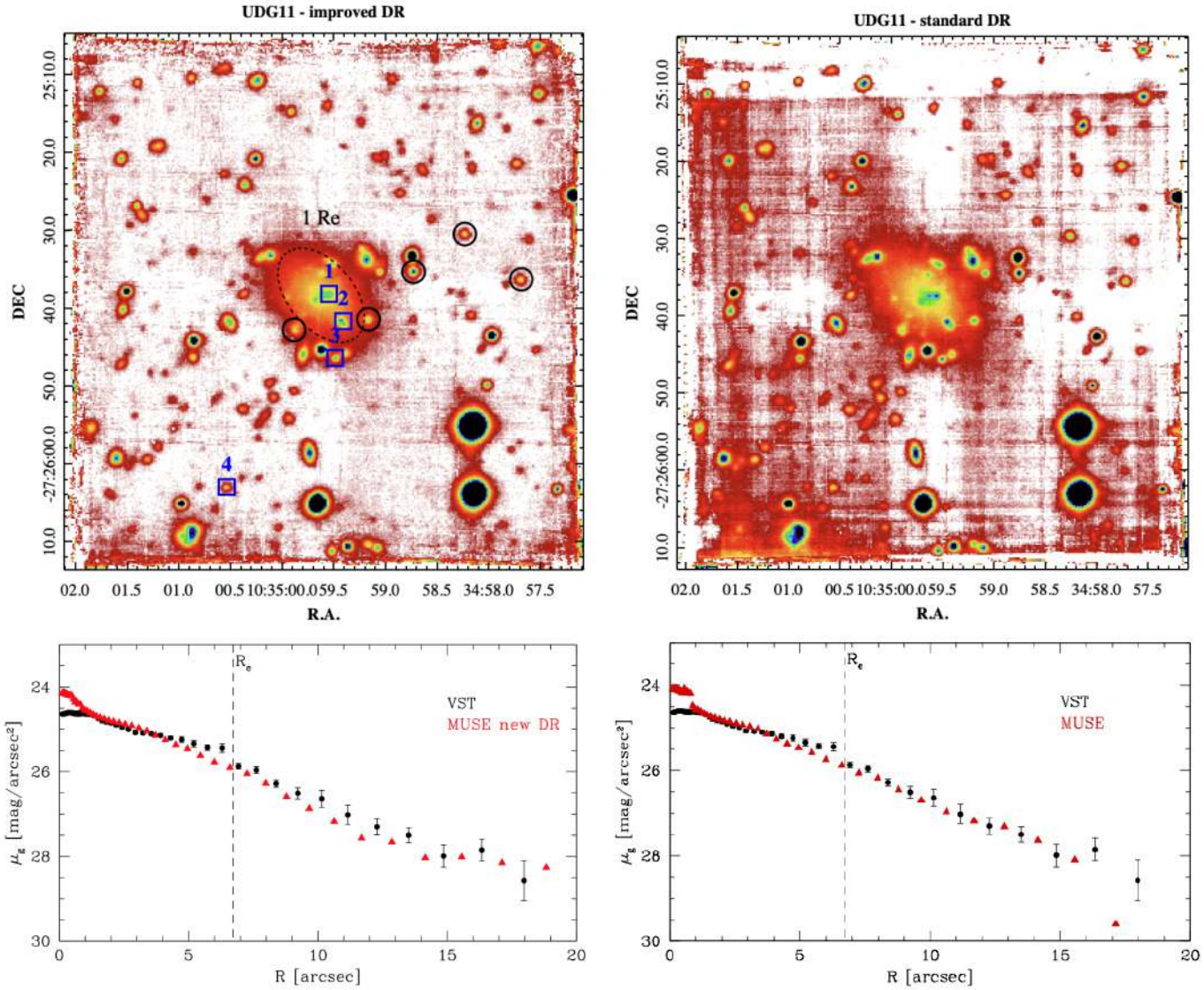

Fig. 3. MUSE reconstructed image of UDG11. Top panels: reconstructed images obtained by improving the sky subtraction (left panel) as described in Sect. 3.2, and with the standard prescriptions for the data reduction (right panel). In the left panels, the dashed ellipse marks the isophote at $1R_e$. The confirmed GCs are marked with the blue numbered boxes; see also Table 3. GCs 1 and 3 have radial velocities that are consistent with UDG11, while GCs 2 and 4 have radial velocities that are inconsistent with UDG11 but still consistent with the Hydra I cluster. The photometrically preselected GC candidates from Iodice et al. (2020) are marked with black circles. Four of them were found to be emission-line galaxies, and for the other one it was not possible to retrieve the V_{sys} due to the low S/N (see Sect. 5.5 for details). Bottom panels: azimuthally averaged surface-brightness distribution derived from the MUSE reconstructed image (red triangles) compared with the same profile derived from the VST optical *g*-band image (black circles) obtained by improving the sky subtraction (left panel) and with the standard prescriptions for the data reduction (right panel). In both panels, the difference between VST and MUSE surface-brightness profiles inside ∼1 arcsec is due to the seeing-limited observations of the optical VST images.

accounting for varying sky backgrounds[2]. After applying these factors to the pixtables of the individual exposures, we combined them with the standard ESOREFLEX workflow.

Additional cleaning of the residual sky contamination was performed on the final stacked datacube using the Zurich Atmospheric Purge algorithm (ZAP; Soto et al. 2016). We ran ZAP within the ESOREFLEX environment, where a dedicated workflow is available within the MUSE pipeline. We parsed the custom sky mask to the workflow and tested different parameter combinations to obtain the optimum sky-subtraction results. The reconstructed images of the final sky-subtracted data cube for UDG11 – obtained with the standard prescriptions for the sky subtraction and with the improved method described above – are shown in Fig. 3. The reconstructed images are displayed with the same intensity levels, which emphasises the improvement in the background level residual noise in our adopted 'improved data reduction' (see top left panel of Fig. 3) with respect to the cube reduced with the standard sky-subtraction technique (top right panel of Fig. 3).

[2] This workflow is not ingested into the ESOREFLEX pipeline; we acknowledge here a private communication with Lodovico Coccato at ESO.

4. Cluster membership

The first goal of the LEWIS project is to confirm the cluster membership of all targets in the sample. To this aim, for

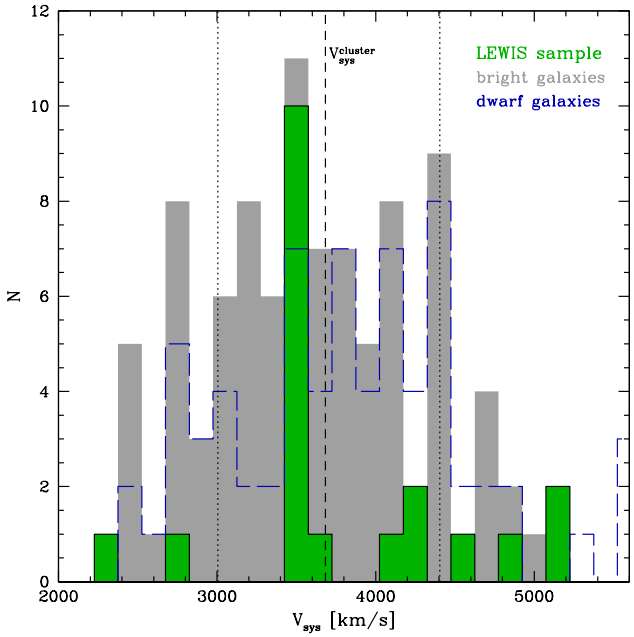

Fig. 4. Velocity distribution of the galaxies in the LEWIS sample (green histogram). The distribution of velocities for the bright cluster members ($m_B < 16$ mag) and for the dwarf galaxy population in the Hydra I cluster are shown with the grey and long-dashed blue histograms, respectively, from the catalogue by Christlein & Zabludoff (2003). The vertical dashed line marks the cluster mean velocity of $3683 \pm 46\,km\,s^{-1}$. The vertical dotted lines correspond to the average velocity dispersion of the cluster members, namely $\sim 700\,km\,s^{-1}$ (Lima-Dias et al. 2021).

each galaxy, we derived the systemic velocity (V_{sys}) by fitting the stacked spectrum inside $1R_e$ with the penalised PiXel-Fitting code (pPXF; Cappellari 2017) using the MUSE rest-frame wavelength range between 4800 and 7000 Å. During this step, the region of the spectrum at longer wavelengths is excluded, because these latter are strongly affected by residuals from the sky line subtraction. Before obtaining the stacked spectrum, we used the MUSE reconstructed image to mask all the background and foreground bright sources. In addition, in the stacked spectrum, we also masked all those wavelength regions with strong sky residuals. The MUSE reconstructed images and the stacked spectra for all the LEWIS galaxies observed so far are shown in Appendix A.

We used the E-MILES single stellar population (SSP) models (Vazdekis et al. 2012, 2015) as spectral templates. These have a spectral resolution of $FWHM = 2.51$ Å (Falcón-Barroso et al. 2011) and cover a large range in age (from 30 Myr to 14 Gyr) and total metallicity ($-2.27 \leq [M/H] \leq 0.4$ dex). The error estimate for each value of V_{sys} corresponds to the formal error provided by pPXF. The V_{sys} value for each of the observed galaxies is reported in Table 1.

The distribution of V_{sys} values is plotted in Fig. 4. It ranges from $2317\,km\,s^{-1}$ to $5198\,km\,s^{-1}$, with a peak value around $\sim 3500\,km\,s^{-1}$, which coincides with the peak of the velocity distribution for the Hydra I bright ($m_B \leq 16$ mag) cluster members and dwarf galaxy population. The mean cluster velocity, $V_{sys} = 3683 \pm 46\,km\,s^{-1}$ (Christlein & Zabludoff 2003), and its velocity dispersion, $\sigma_{cluster} \sim 700\,km\,s^{-1}$ (Lima-Dias et al. 2021), can be used to determine the membership of our targets: 14 of the 20 galaxies with the measured velocities are cluster members because they are found to have their velocity within the cluster velocity dispersion ($3438 \leq V_{sys} \leq 4302\,km\,s^{-1}$). As the cluster is quite isolated in the recession velocity space between 2000 and $5000\,km\,s^{-1}$ (Richter et al. 1982; Richter 1987), and the velocity distribution of its galaxy members is broad, the three galaxies with velocities inside $2\sigma_{cluster}$ are also likely cluster members (UDG4, UDG8 and UDG12, see Table 1). The three remaining galaxies, UDG22 with $V_{sys} = 5198 \pm 5\,km\,s^{-1}$, LSB6 with $V_{sys} = 5193 \pm 5\,km\,s^{-1}$, and LSB8 with $V_{sys} = 2718 \pm 5\,km\,s^{-1}$, could be background or foreground galaxies.

In the photometric work of Iodice et al. (2020) and La Marca et al. (2022a), to discriminate UDGs from normal dwarf LSB galaxies by their physical sizes, we assumed that all newly detected galaxies are at the distance of the Hydra I cluster (i.e. 51 Mpc). Now, having confirmed the cluster membership of most UDGs and LSB galaxies with our LEWIS spectroscopy, we use a fixed distance when deriving their effective radii and confirming their morphological classification, as already published in our previous papers (see also Table 1). We are aware that the Hydra I cluster might have a physical depth of a few megaparsecs, and therefore some of the UDGs might be located in front of or behind the cluster, resulting in size differences of ±4% for a relative distance of 2 Mpc with respect to Hydra I.

For the three outliers in the redshift distribution, we used the Hubble law – assuming $H_0 = 70\,km\,s^{-1}$/Mpc – to derive the Hubble flow distance based on the measured V_{sys}. For UDG22 and LSB6, we obtained a distance of 74 Mpc and the new values for their effective radius are $R_e = 5.22$ kpc and $R_e = 5.80$ kpc, respectively. For LSB8, which has a lower V_{sys}, $R_e = 1.12$ kpc. Therefore, we find UDG22 and LSB6 to be more diffuse and fainter, if they are indeed a UDG and a LSB in the background of the Hydra I cluster. LSB8 is smaller, and according to its central surface brightness $\mu_{0,g} = 23.20\,mag\,arcsec^{-2}$ can be classified as a foreground dwarf galaxy.

5. Data quality and preliminary results: UDG11 as a test case

This section describes the analysis of the MUSE data for one of the sample galaxies, UDG11, in order to assess the data quality. UDG11 was chosen as a test case because it is one of the faintest and most diffuse galaxies in the sample, with a comparably large number of photometrically detected GC candidates (see Table 1), for which we obtained all the requested data at the desired depth. With this target, we customised and tested the data reduction process as well as the analysis tools and methods that were subsequently applied to the entire LEWIS sample. In the following sections, we describe the analysis of the MUSE cube for UDG11 and how we derived the *(i)* line-of-sight velocity distribution LOSVD, *(ii)* the stellar population properties, and *(iii)* the systemic velocities of the GC candidates.

UDG11 is located on the western side of the cluster (see Fig. 2). The structural properties for this galaxy – based on deep images – were published by Iodice et al. (2020). More specifically, UDG11 has an absolute magnitude of $M_r = -14.75$ mag in the r band and a stellar mass of $M_\star = 0.63 \times 10^8\,M_\odot$. The structural parameters derived from the 1D fit of the azimuthally averaged surface brightness profiles in the g band are $\mu_{0,g} = 24.36 \pm 0.13\,mag\,arcsec^{-2}$ and $R_e = 1.66 \pm 0.12$ kpc. The integrated colour is $g - r = 0.43 \pm 0.11$ mag. Based on the colour selection and shape, the estimated total number of GCs[3] in this galaxy is $N_{GC} = 7 \pm 3$ (see Iodice et al. 2020, and Table 1).

[3] Here and throughout the paper, N_{GC} is the total number of GCs hosted in the galaxy obtained after photometric and spatial incompleteness correction, as described in Sect. 2.1 of Iodice et al. (2020).

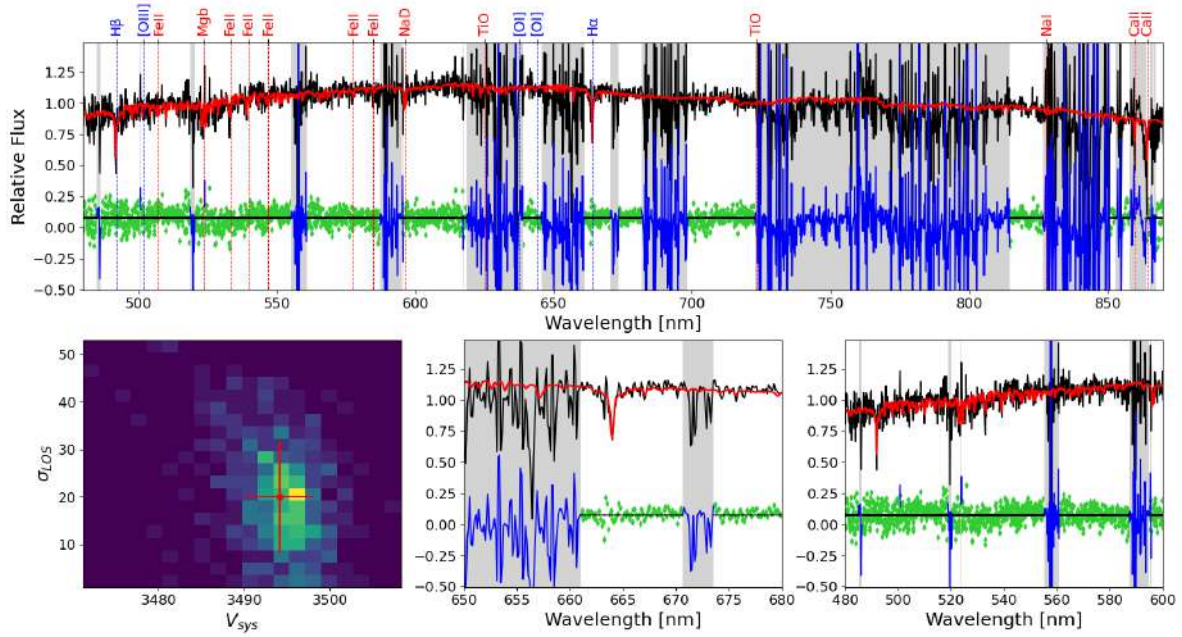

Fig. 5. Restframe stacked MUSE spectrum (black solid line) for UDG11 derived inside $1R_e$. The main absorption features are marked as dashed red (absorption features) and blue lines (absorption features, but potentially also in emission) and labels. The red solid line represents the best fit obtained with pPXF. Green points are the residuals between the observed spectrum and its best fit. The grey areas are the masked regions of the spectra and are excluded from the fit. Bottom (right and middle) panels show the enlarged regions around the main fitted absorption features of the top-row fit in the optical wavelength range 4800–7000 Å. The lower-left panel shows the grid of values for the LOS velocity (V_{LOS}) and velocity dipersion (σ_{LOS}) derived from the Monte Carlo simulations (see text for details).

The MUSE cube obtained for UDG11 has a total integration time of 6.10 h. The MUSE reconstructed images (from the whole wavelength range) resulting from the standard data reduction and improved procedure (see Sect. 3.2) are shown in Fig. 3. In the lower panels we compare the azimuthally averaged surface brightness profiles from the MUSE reconstructed images with that of the optical VST image in the g band after arbitrarily rescaling the data. This illustrates that with the MUSE data for UDG11, we are able to map the integrated light down to $\mu_g \sim 28$ mag arcsec^{-2} and out to $\sim 2R_e$, which also suggests that a satisfactory level of sky subtraction has been achieved. With the improved data reduction, the residual patterns of the MUSE slices are well removed, even if the continuum appears slightly over-subtracted when compared to photometric profiles (Fig. 3).

From the MUSE cube obtained with the improved data reduction and used for the analysis described in this paper, we extracted the stacked spectrum inside a circular area with a radius of $R = 1R_e$, where all bright sources (background galaxies and foreground stars) are masked. This is shown in Fig. 5. It is worth noting that the S/N per spaxel of the stacked spectrum from this cube is $S/N = 16$, which is higher than the $S/N = 12.6$ we computed for the spectrum from the standard data reduction. In addition, by masking the wavelength regions affected by the sky-line residuals, the S/N increases to 20.

In this spectrum, we can clearly identify the absorption features of the most relevant lines: Hβ, Mgb, Hα, and the CaT (see also lower boxes in Fig. 5). On the other hand, we do not detect emission lines, suggesting that this galaxy is devoid of ionised gas.

5.1. Stellar kinematics

We derived the stellar kinematics of UDG11 using the pPXF code. Specifically, we extract the LOSVD, which is parametrised by the line-of-sight (LOS) velocity V, velocity dispersion σ, and Gauss-Hermite moments h_3 and h_4 (Gerhard 1993; van der Marel & Franx 1993). We used the E-MILES stellar library (Vazdekis et al. 2016) with SSP models as spectral templates. These models have a spectral resolution comparable to the average of the MUSE spectra, namely ∼2.5 Å (see Sect. 3), which makes them suitable for our purposes. For all models, we assume a Kroupa IMF (Kroupa 2001).

To assess the effectiveness of the MUSE cube and identify any potential constraints in measuring stellar kinematics caused by the low surface-brightness levels of these galaxies, we examined the entire MUSE rest-frame wavelength range from 4800 to 9000 Åas well as a restricted range from 4800 to 7000 Å, which is less susceptible to the residual effects of sky-line subtraction.

As a reliable extraction of the higher-order Gauss-Hermite moments requires a relatively high S/N (e.g. Gadotti & de Souza 2005, see also Fig. 7 of this study for exact estimations), for UDG11 we derived only the first two moments of the LOSVD, namely V and σ. These quantities were estimated by running pPXF to fit the 1D stacked spectrum inside $1R_e$. On the full MUSE rest-frame wavelength range between 4800 and 9000 Å, the best fit was obtained by allowing high-order multiplicative and additive Legendre polynomials of degree 10. Including additive polynomials allows us to correct for differences in the flux calibration and overcome the limitations of the stellar library, whereas multiplicative polynomials directly alleviate imperfections in the spectral calibration affecting the continuum shape. Results are shown in Fig. 5. A similar approach was already used for the UDG NGC1052-DF2 by Emsellem et al. (2019) to estimate the stellar kinematics from MUSE data. The mean LOS velocity (which we adopted as systemic velocity) and velocity dispersion of UDG11 are $V_{sys} = 3507 \pm 3$ km s^{-1} and $\langle\sigma\rangle_e = 20 \pm 8$ km s^{-1}, respectively. Restricting the fit to the range

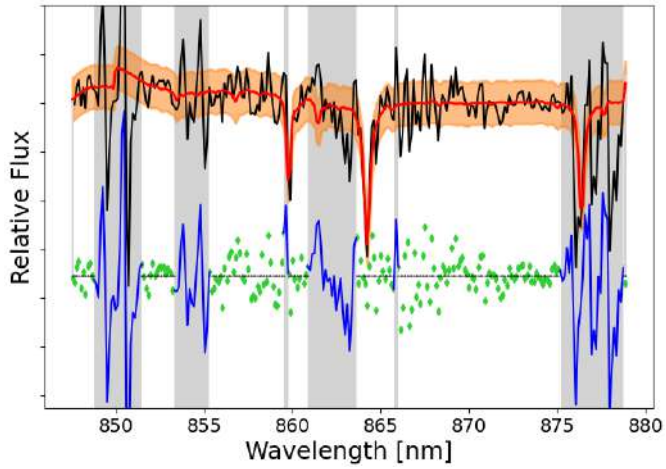

Fig. 6. Stacked MUSE spectrum for UDG11 in the CaT region inside $1R_e$. The red solid line represents the best fit obtained with pPXF. Green points are the residuals between the observed spectrum and its best fit. The grey areas are the masked regions of the spectrum, which are excluded from the fit. The orange region corresponds to the standard deviation of the best fit across all ∼1400 iterations.

4800–7000 Å, the best fit provides $V_{sys} = 3509 \pm 3\,km\,s^{-1}$ and $\langle\sigma\rangle_e = 20 \pm 10\,km\,s^{-1}$, which are consistent with the former values.

Estimates of the error on V_{sys} and $\langle\sigma\rangle_e$ are obtained by performing Monte Carlo simulations (e.g. Cappellari & Emsellem 2004; Wegner et al. 2012). This procedure is described in Appendix B.

The stacked spectrum for UDG11 shows prominent absorption CaT lines (see Fig. 6). These lines are the strongest features in the stellar continuum for a large variety of stellar types (Cenarro et al. 2001) in addition to being at the MUSE wavelength region with the best resolution (Bacon et al. 2017); they are therefore particularly suitable for extraction of the stellar kinematics. We ran pPXF on the wavelength region restricted to the rest-frame interval 8475–8690 Å. To fit the CaT region exclusively, we used the CaT templates by Cenarro et al. (2001). Given that the spectral resolution of these templates is ∼1.5 Å, they were convolved to the resolution of the MUSE spectra in this range (∼2.5 Å). The best fit shown in Fig. 6 was obtained with multiplicative and additive Legendre polynomials of degree 7, and by masking the reddest CaT lines, which are strongly affected by a residual of the sky lines. We obtain $V_{sys} = 3501 \pm 5\,km\,s^{-1}$ and $\langle\sigma\rangle_e = 16 \pm 12\,km\,s^{-1}$. These values are consistent with the previous estimates provided above, despite the fact that $\langle\sigma\rangle_e$ has a larger error. All quantities computed with the three different methods are reported in Table 2.

5.2. Tests on the velocity dispersion measurements

By fitting the stacked spectrum inside $1R_e$, we derived a very low value for $\langle\sigma\rangle_e$ of $\sim 20\,km\,s^{-1}$, which is less than the spectral resolution of MUSE (see Sect. 3). As stated in the previous section, the fit was performed using the latest version of the pPXF code developed by Cappellari (2017). This author showed that, for spectra with high S/N ($S/N > 3000$ per spectral element), the full spectrum fitting provides reliable kinematics at any velocity dispersion, even below the instrumental resolution of MUSE.

Using the SAMI integral-field spectrograph to study the dwarf galaxies in the Fornax clusters, Eftekhari et al. (2022) demonstrated that, with a velocity dispersion of ∼0.4, the instrumental resolution can be measured at $S/N = 15$ with an accuracy of ∼20%–30%.

The LEWIS data are in the low-surface brightness regime, and therefore the main issue is the S/N of the spectra. We therefore performed several tests to identify the minimum S/N needed for the data to retrieve a reliable value for σ_{LOS}. We simulated mock spectra based on the E-MILES models, with different S/N ranging from 5 to 120 by introducing Poissonian noise. A full description of this test is reported in Appendix D.1. We find that from spectra with $S/N \sim 15$–20 (comparable to that of the stacked spectrum of UDG11), we can retrieve a velocity dispersion as low as $\sigma_{LOS} \sim 10\,km\,s^{-1}$ with an uncertainty of $10\,km\,s^{-1}$. Results are shown in Fig. 7. Similar tests were performed by Eftekhari et al. (2022), and we found consistent results.

In conclusion, our tests demonstrate that we need a minimum S/N per spaxel of 10 for an unbiased velocity determination. Given that the stacked spectrum of UDG11 has $S/N = 16$, the best-fit value for its velocity dispersion is $\langle\sigma\rangle_e = 20 \pm 8\,km\,s^{-1}$. This might be considered an upper limit because we cannot exclude lower values.

In addition to the tests described above, we independently calculated the expected value of the velocity dispersion for UDG11. By adopting the scaling relation derived by Zaritsky & Behroozi (2023), where the total mass-to-light ratio Γ_e derived inside R_e (Γ_e) is a function of the velocity dispersion and the effective luminosity I_e, we derived $\sigma = 19.97\,km\,s^{-1}$. In this relation, we use $L_e = 3.35 \times 10^7\,L_\odot$ derived by Iodice et al. (2020), and we assume a total $M/L = 10$, which is constant with radius and typical for dwarf galaxies of comparable luminosity to UDG11 (e.g. Battaglia & Nipoti 2022). The resulting value of the velocity dispersion is fully consistent with the estimate obtained by fitting the MUSE cube. Therefore, even considering the limits of the data described above, we conclude that the derived estimate of the velocity dispersion for UDG11 is very close to the expected value for this galaxy.

5.3. Spatially resolved stellar kinematics maps

The 2D map of the stellar kinematics is derived using the modular Galaxy IFU Spectroscopy Tool (GIST) pipeline developed for the analysis of IF spectroscopic data by Bittner et al. (2019). Using GIST, we spatially binned the datacube spaxels with the adaptive algorithm by Cappellari & Copin (2003) based on

Table 2. Stellar kinematics, age, and metallicity derived for UDG11 from the LEWIS data.

Fit	λ range	V_{sys}	$\langle\sigma\rangle_e$	$[M/H]$	Age
	[Å]	[km s^{-1}]	[km s^{-1}]	[dex]	[Gyr]
(1)	(2)	(3)	(4)	(5)	(6)
1D	4800–9000	3507 ± 3	20 ± 8	-1.2 ± 0.1	10 ± 1
1D	8475–8690	3501 ± 5	16 ± 12	–	–
2D	4800–7000	3532 ± 43	27 ± 8	–	–
GC1	4800–9000	3503 ± 12	–	-0.7 ± 0.3	9 ± 2

Notes. In Cols. 1 and 2 we report the kind of fit we performed or source we used and the wavelength range used to derive the stellar kinematics, age, and metallicity, respectively. Columns 3 and 4 list the systemic velocity and velocity dispersion derived for UDG11 inside $1R_e$ (see Sect. 5.1). In Cols. 5 and 6 we report the estimates of the metallicity and age derived for UDG11 inside $1R_e$ (see Sect. 5.4), and for GC1.

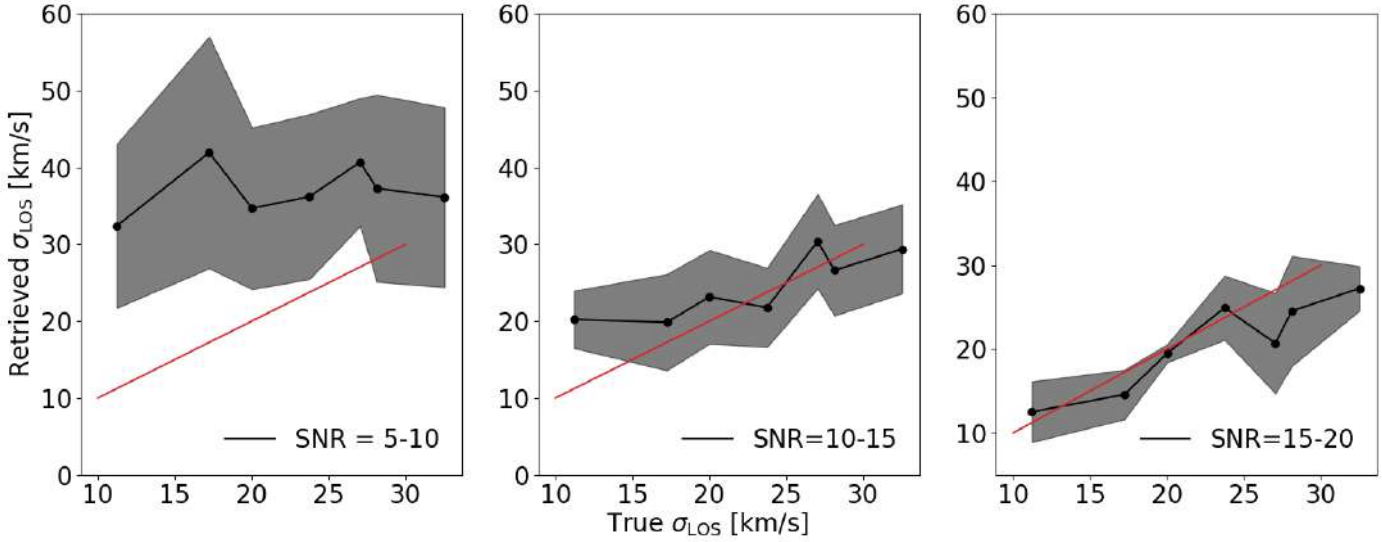

Fig. 7. Results of simulations testing the ability of our pipeline to successfully recover a velocity dispersion of different values at low S/N (per pixel) levels, from S/N = 5–10 (left panel), S/N = 10–15 (middle panel), up to S/N = 15–20 (right panel). Shaded areas correspond to the standard deviation of the measured values at every S/N. The red solid line corresponds to the output values equal to the input ones (unity line). In this experiment, the error is dominated by Poisson noise and no systematic sources of uncertainties have been considered. See Appendix D.1 for details.

Voronoi tessellation. As the average S/N of the stacked spectrum is ∼16, we adopted S/N = 10 as the binning threshold (Fig. 8, left panel). The fit was restricted to the optical wavelength range 4800−6800 Å in order to avoid the region of the CaT affected by the sky-line residuals, particularly in the galaxy outskirts. As starting guesses, we used the same 'setup' as that used for the best fit of the 1D stacked spectrum inside $1R_e$. Therefore, we adopted the E-MILES stellar templates, additive polynomials of grade 10, and multiplicative polynomials of grade 10. Figure 8 shows the map of the Voronoi bins, with the average signal-to-residual noise ratio S/rN (left panel), the resulting 2D maps of the LOS velocity V_{LOS} (middle panel), and velocity dispersion σ_{LOS} (right panel). The S/N map shows that all bins close to the centre of the galaxy, corresponding to the brightest regions, have $S/N \geq 10$ per spaxel, which is the targeted threshold fixed for the Voronoi tessellation. In the galaxy outskirts, some bins have $S/N \leq 10$ per spaxel. This effect was discussed by Sarzi et al. (2018, see Fig. 6 of that paper and references therein) for the MUSE cubes. These latter authors found that the quality of the Voronoi-binned spectra decreases with surface brightness, where lower values of the S/N with respect to the formal threshold chosen for the Voronoi bins are found at the lowest surface-brightness levels. This is due to the impact of the spatial correlations between adjacent bins at lower surface brightness levels.

From the 2D map of the LOS velocity dispersion (Fig. 8, right panel), we extracted the effective velocity dispersion $\langle\sigma\rangle_e$ by calculating the weighted mean of the values enclosed in an elliptical region with a semi-major axis equal to the effective radius and with axial ratio $q = 1 - \epsilon$, with ellipticity $\epsilon = 0.3$. The associated error was estimated by calculating the standard error of the weighted mean. We found $\langle\sigma\rangle_e = 27 \pm 8\,\mathrm{km\,s^{-1}}$, which is consistent within 1σ error with the different estimates derived from the 1D spectrum (Table 2). However, we also tested more options where the degree of Legendre polynomials spans a larger range of values from 5 to 14. The resulting values of $\langle\sigma\rangle_e$ are shown in Fig. 9. In order to be consistent with the stellar kinematics derived from the 1D stacked spectrum, we adopted the 2D maps obtained with the same multiplicative and additive polynomials (Fig. 8).

The 2D V_{LOS} map does not show a clear trend of rotation along any direction, the 2D σ_{LOS} map shows values ranging from $\sigma_{LOS} \sim 10\,\mathrm{km\,s^{-1}}$ to $\sigma_{LOS} \sim 30\,\mathrm{km\,s^{-1}}$ along the major axis, and larger values of $\sigma_{LOS} \sim 40$–$50\,\mathrm{km\,s^{-1}}$ along the minor axis of the galaxy. We checked the reliability of these measurements by inspecting the fit of the spectrum in each bin. We found that some bins in the outskirts have a lower S/N with respect to the adopted threshold for the Voronoi binning, and therefore in these bins, the values of σ_{LOS} are affected by a systematic overestimation, as addressed in Sect. 5.1 (see Fig. 7).

5.4. Stellar populations

For UDG11, we performed an additional pPXF run on the stacked spectrum inside $1R_e$ in order to derive its mean age and total metallicity. We fitted the full MUSE rest-frame wavelength range between 4800 and 9000 Å using the E-MILES templates (Padova isochrones with Kroupa IMF; Girardi et al. 2000). As a first step, we generated a reference fit to be used as a central setting for the generation of bootstrapped spectra and as a reference for Monte Carlo iterations over various parameters (see Appendix B). This step involves the creation of a mask, flagging all noisy pixels and sky lines affecting the spectra (with a flux greater than three times the noise level). The process also includes setting polynomial degrees as shown in Sect. 5.1: we use the same framework as that used for the 1D stacked spectrum, but with the exclusion of additive polynomials. In addition, we also fix our previously found 1D kinematic solutions to those from the stellar population fits, thus constraining the velocity dispersion.

To construct the final solution, pPXF uses a technique called regularisation, which allows the routine to preferentially select the smoothest solution among many (products of the well-known age–metallicity degeneracy; see e.g. Cappellari 2017). Over 700 iterations, the median age and metallicity that we obtained by fitting the whole MUSE wavelength range are

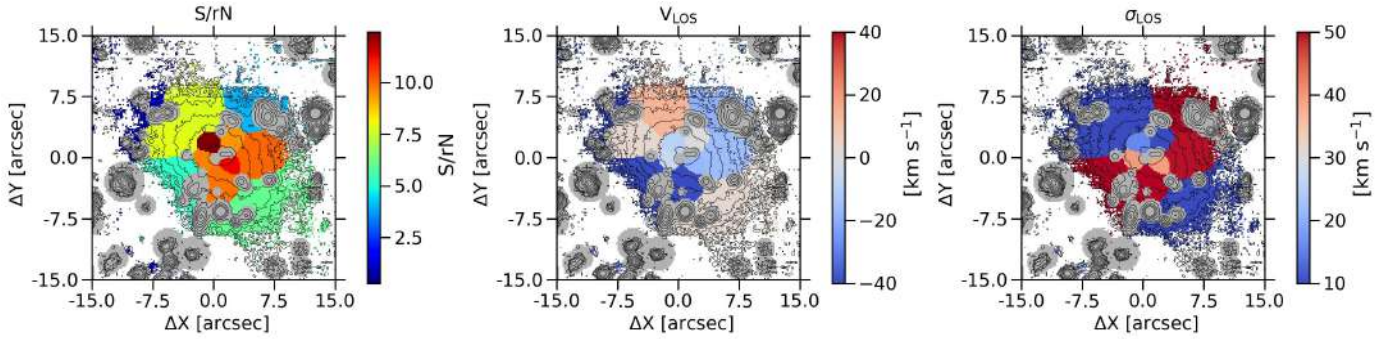

Fig. 8. Two-dimensional kinematic maps of UDG11: Signal-to-residual noise ratio S/rN (left), LOS velocity V_{LOS} (centre), and velocity dispersion σ_{LOS} (right) derived from a Voronoi binning with $S/N = 10$. Contours correspond to the isophotes of the light distribution. Grey circles represent the adopted mask. The FoV is 30×30 arcsec and is oriented with north at the top and east to the left.

Age = 10 ± 1 Gyr and $[M/H] = -1.17 \pm 0.11$ dex, respectively. By fitting the stacked spectrum for one of the confirmed GCs (see Sect. 5.5), we obtained comparable age (7.9 ± 1.5 Gyr) and metallicity ($[M/H] = -0.7 \pm 0.3$ dex). Results are plotted in Fig. 10 (left panel) and listed in Table 2.

As a self-consistency check, we take the E-MILES set of templates (BaSTI isochrones with the same Kroupa IMF) and compute the Lick Hβ and [MgFe]′ indices of various templates in order to construct a reference grid. This computation is done with the latest version of pyphot[4] without following the usual Lick index convention (see e.g. Vazdekis et al. 2010) for the assumed FWHM. Instead, to avoid losing potentially useful information, we keep the resolution of the data intact, as it roughly matches that of the templates used to construct the grid. To compute the errors on the Lick indices, we take Lick measurements for every best-fit model from each converging pPXF iteration, and then use the 1σ measurement on the Monte Carlo distribution to estimate the error. We find the Lick index measurements to be relatively consistent (Lick Hβ = 2.54 ± 0.2 and [MgFe]′ = 1.49 ± 0.1) with the stellar population measurements of age and metallicity. Results are shown in Fig. 10 (right panel).

5.5. Globular cluster population

From the UDG11 MUSE cube, we extracted and analysed the spectra of the photometrically pre-selected GC candidates from Iodice et al. (2020), as well as all other point-like sources within the luminosity range expected for GCs (see also Fig. 3). Where the S/N was sufficient, we measured the radial velocity to verify their kinematical association with the UDG.

We only considered the sources with $S/N \geq 2.5$ in the background-subtracted spectrum using an eight-pixel circular aperture. For lower S/N, the V_{sys} could not be reliably determined. This S/N limit corresponds to an apparent magnitude of $m_g \sim 25.5$ mag, about 0.5 mag brighter than the expected turnover magnitude (TOM) of the GC luminosity function (GCLF) at the distance of the Hydra I cluster (Iodice et al. 2020).

In order to measure the radial velocity of the candidate GCs, we used the SSP model spectra from the E-MILES[5] library to fit each GC spectrum with pPXF. In this case, we used an IMF with a double power-law (bimodal) shape and a high mass slope of 1.30 (Vazdekis et al. 1996). We did not attempt to measure the intrinsic velocity dispersion of the candidate GCs because of the low spectral resolution of MUSE and the limited S/N of the observed spectra (see also Fig. 7).

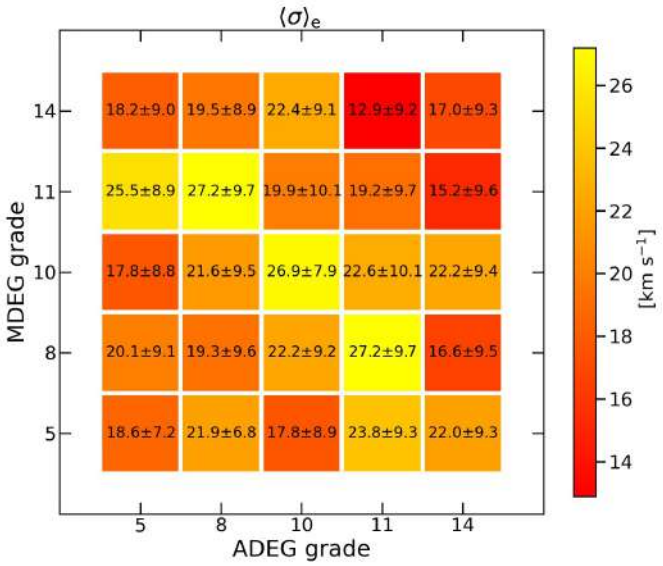

Fig. 9. Values of the weighted mean of $\langle\sigma\rangle_e$ derived from the fit of the Voronoi binned cube (with $S/N = 10$ per spaxel) for different degrees of multiplicative and additive Legendre polynomials. Boxes are colour coded according to the value of $\langle\sigma\rangle_e$. See text for details.

Figure 11 shows the spectrum of one GC in the field, and the corresponding pPXF fit as an example. The regions excluded from the spectrum are grey-shaded and correspond to the residual sky or telluric lines. Moreover, we excluded the wavelength region with $\lambda \geq 7000$ Å from the fit because of the presence of strong sky residuals, which rendered the identification of the CaT unfeasible.

Also in this case, to calculate a reliable uncertainty on the estimate of V_{sys}, we fitted the sources with an approach based on the Monte Carlo technique (see Sect. 5.1). After the first fit using the original spectrum, we created 200 realisations with the same S/N as the original spectrum by perturbing the noise-free best-fit spectrum[6] with random draws in each wavelength bin from the residual (best-fit subtracted from the original spectrum). The fit was then repeated and the LOS velocity was determined from the mean of the resulting distribution. The random uncertainty

[4] https://mfouesneau.github.io/pyphot/

[5] We restricted the library to ages ≥8 Gyr. According to Fahrion et al. (2020), this choice appears reasonable because most GCs have ages >8 Gyr with only very rare exceptions.

[6] By 'best-fit spectrum', we refer to the best-fitting template spectrum.

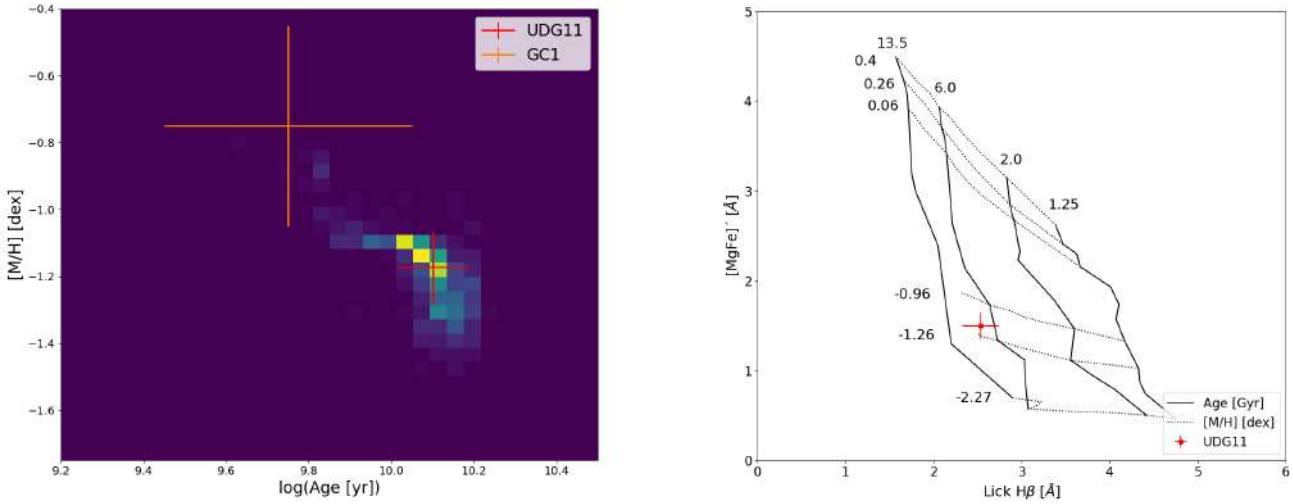

Fig. 10. Mean age and metallicity for UDG11 derived from the stacked spectrum inside $1R_e$. Left panel: best fit derived using the pPXF code. The red cross corresponds to the values for age and metallicity (including errors) obtained by the best fit on the whole MUSE spectral range. The orange cross shows the average age and metallicity (including errors) for one of the confirmed GCs in UDG11 (see Sect. 5.5). Right panel: lick index measurements. Using the E-MILES BaSTI templates, we constructed the grid: vertical dashed lines denote models for the same age (left being the oldest), and horizontal dotted lines refer to model measurements for spectra with the same metallicity (with the most metal-poor ones located at the lower part).

Table 3. Identified GCs in the UDG11.

GC	RA	Dec	V_{sys}	ΔV	m_r	S/N	Galactocentric distance	Classification
	[deg]	[deg]	[km s^{-1}]	[km s^{-1}]	[mag]		[kpc]	
(1)	(2)	(3)	(4)	(5)	(6)	(7)	(8)	(9)
1	158.7482	−27.427	3503 ± 12	−4 ± 13	24.57 ± 0.07	10.2	$<R_e$	GC/Nucleus
2	158.7477	−27.4280	3767 ± 54	+260 ± 54	24.05 ± 0.07	5.8	$<R_e$	Intra-cluster GC?
3	158.7479	−27.4293	3460 ± 21	−47 ± 22	24.18 ± 0.08	4.5	$<1-2Re$	GC
4	158.7523	−27.4339	3640 ± 33	+133 ± 34	24.88 ± 0.03	2.7	$\sim 4R_e$	Intra-cluster GC?

Notes. Column 1: GC number as marked in Fig. 3. Columns 2 and 3: coordinate of the sources. Column 4: estimated line-of-sight velocity and uncertainty. Column 5: difference between the estimated radial velocity of the sources and the radial velocity of the UDG11. We adopted as radial velocity for the UDG11 the value reported in Sect. 5. Column 6: magnitude in the r-band from the VST photometry. Column 7: S/N per pixel of the background-subtracted spectrum. Column 8: distance of the sources in terms of the effective radius of the UDG. Column 9: source classification.

is given by the standard deviation assuming a Gaussian distribution. A detailed description of the method used to study the GC population in UDGs, including UDG11, is the subject of a forthcoming paper by Mirabile et al. (in prep.).

We identified four point sources in the UDG11 cube with a V_{sys} velocity consistent with that of the Hydra I cluster; these are listed in Table 3 and marked in Fig. 3. The projected positions of GC1, GC2, and GC3 are within $2R_e$ of UDG11, while GC4 is much more distant ($\sim 4R_e$).

The radial velocities of GC1 and GC3 are 3503 ± 12 km s^{-1} and 3460 ± 21 km s^{-1}, respectively. Compared to the systemic velocity of the UDG11, these are within 1σ and $\sim 2\sigma$, respectively. We therefore consider that both GCs are associated to UDG11. Moreover, it is worth noting that the velocity differences ΔV of GC1 and GC3 with respect to the V_{sys}, of $\Delta V \sim -4 \pm 13$ km s^{-1} and $\Delta V \sim -47 \pm 22$ km s^{-1} (see Table 3), respectively, are consistent with the stellar velocity dispersion obtained for UDG11 close to the centre ($\sigma_{LOS} \sim 20$ km s^{-1}) and in the southeast region of the galaxy ($\sigma_{LOS} \sim 20-40$ km s^{-1}), as shown in Fig. 8.

The velocity difference $\Delta V \geq 130$ km s^{-1} for GC2 and GC4 might suggest they are not gravitationally bound, and these two GCs could therefore be considered as intra-cluster GCs. However, this result can only be confirmed once the DM content of this galaxy is better constrained. To this aim, we calculated the escape velocity, assuming a NFW halo profile (Miller et al. 2016), and estimated the DM halo mass using the Burkert & Forbes (2020) relation. We found that, if the DM halo mass lies between 4 and $6 \times 10^{10}\, M_\odot$, the GCs with an escape velocity of ≤ 200 km s^{-1} can be considered as bound systems. Therefore, GC2 with $\Delta V \simeq 260$ km s^{-1} should be considered an intra-cluster GC, whereas all the other GCs could potentially be bound to the UDG11. Finally, the very central GC, GC1, might be a nuclear star cluster.

In summary, the preliminary analysis of the GC systems in UDG11 suggests that this galaxy has either two or three spectroscopically confirmed GCs that are bound to the host. By excluding GC1 as a potential nuclear star cluster and GC2 as an intra-cluster GC, with the remaining two spectroscopically confirmed GCs we can estimate the GC specific frequency (S_N) of UDG11. Our spectroscopic completeness limit is $m_g \sim 25.5$ mag ($m_r \sim 24.9$ mag), which is 0.5 brighter than the GCLF turnover magnitude of $m_g^{TOM} = 26$ mag (Iodice et al. 2020). Assuming a GCLF width of $\sigma_{GCLF} = 1$ mag (Villegas et al. 2010), our spectroscopic completeness limit therefore corresponds to 34% of the GCLF. The incompleteness-corrected total number of

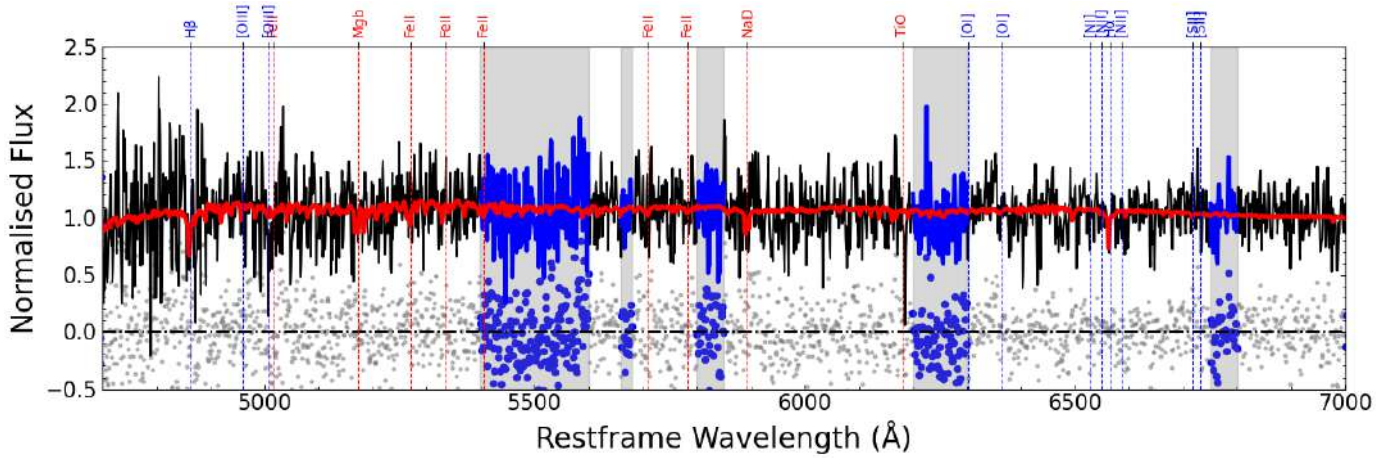

Fig. 11. Stacked spectrum of GC3, with $S/N \sim 4.5$ Å^{-1}. The original spectrum is shown in black, and the pPXF fit is in red. Regions with strong sky residual lines were masked from the fit (grey-shaded areas).

GCs is therefore $2/0.34 = 5.9^{+2.2}_{-1.8}$, where the error range comes from the 68% confidence interval of a Poisson distribution centred on 3.9 (i.e. the two spectroscopically confirmed GCs have no errorbar, only the incompleteness correction of 3.9 has an error). The absolute V-band magnitude of UDG11 is $M_{V,0} = -14.6 \pm 0.1$ mag. Therefore, we obtain $S_N = 8.4^{+3.2}_{-2.7}$. This value of S_N is consistent with the typical estimates for dwarf galaxies of similar luminosity (Georgiev et al. 2010; Lim et al. 2018). By including both GC1 and GC2, the value of S_N would correspondingly change, but it is still consistent within the uncertainties with the values quoted above.

It is worth noting that none of the five photometrically preselected GC candidates from Iodice et al. (2020, see Fig. 3, black circles) can be confirmed as a GC associated to UDG11: four of them exhibit emission lines typical of background galaxies and one has an insufficient S/N for a reliable velocity measurement. From Iodice et al. (2020), the number of contaminants is 3.3 ± 0.8 arcmin^{-2}, and therefore for a region of $5R_e$ around the UDG11, we expect 3 ± 1 contaminants. Among the five photometrically preselected GCs, we would therefore have expected about two spectroscopically confirmed GCs. This is indeed the case. We note that the majority of photometrically preselected candidates have not been confirmed, while the two newly detected GCs within the MUSE cube did not pass the narrow photometric and morphometric selections adopted for the VST dataset. This is not surprising given the availability of only two photometric and very close optical bands. The preliminary results on other LEWIS targets reveal that UDG11 is rather peculiar in this respect. As an example, out of the five photometric preselected GC candidates of UDG3, three are spectroscopically confirmed GCs, whereas the remaining two have insufficient S/N to provide useful constraints (further details will be presented in Mirabile et al., in prep.).

6. The structure of UDG11 from LEWIS data

In this section, we discuss the stellar kinematics, stellar populations, and DM content of UDG11 resulting from the analysis of the MUSE cube presented in this paper. The main goal is to probe the ability of the LEWIS data to constrain these quantities, the relative uncertainties, and therefore the formation history of UDGs.

6.1. Stellar kinematics and populations of UDG11

Table 2 summarises the measurements of the stellar kinematics (i.e. systemic velocity and velocity dispersion) and the average age and metallicity derived for UDG11 (see Sects. 5.1 and 5.4). Based on the fit of the 1D stacked spectrum inside $1R_e$, these estimates suggest that the UDG11 has a very low velocity dispersion ($\langle\sigma\rangle_e \sim 20$ km s^{-1}), and is old (~10 Gyr) and metal poor ([M/H] ~ −1.2 dex). The spatially resolved map of the LOS velocity (see Fig. 8, central panel) does not reveal a significant velocity gradient or rotation along the photometric axes of the galaxy.

Figure 12 shows the histograms of the stellar mass, velocity dispersion, age, and metallicity measured for UDGs in previous works. The observed values obtained for UDG11 in this paper are also reported for comparison. These plots suggest that the velocity dispersion estimated for UDG11 ($\sigma \sim 20$ km s^{-1}) fits into the broad range of σ values for the majority of UDGs ($8 \leq \sigma \leq 32$ km s^{-1}), which peaks at $\sigma \sim 20$ km s^{-1} (see top-right panel of Fig. 12). Based on the few measurements for the stellar population in UDGs, both age and metallicity span a wide range of values. On average, UDGs seem to be old ($7 \leq$ Age ≤ 14 Gyr) and metal poor ($-1.8 \leq [M/H] \leq -0.5$ dex). However, younger ages (~1–4 Gyr) and subsolar metallicity ([M/H] ~ −0.1 dex) are found for a few objects (see lower panels of Fig. 12). The age and metallicity estimated for UDG11 fit well with the typical values observed for old and metal-poor UDGs.

Figure 13 shows the relationship between velocity dispersion and metallicity as a function of the stellar mass for UDGs. In both panels, UDG11 has comparable values with other UDGs of similar stellar mass, taking into account the uncertainties on both measurements. As already pointed out by Gannon et al. (2021), in the σ–mass relation, the majority of UDGs – including UDG11 – are found in the same region as other dwarf galaxies. However, some UDGs scatter to lower and higher σ values compared to the tighter σ–mass relation of 'normal' dwarf galaxies.

In the mass–metallicity plane, UDGs show a large scatter (see right panel of Fig. 13). Most UDGs, including UDG11, are consistent with the typical values for dwarf galaxies in the same range of masses (Kirby et al. 2013; Simon 2019). Also in this case, metallicities that are both lower ([M/H] ≤ -1.5) and higher ([M/H] ≥ -1) than average are found. In particular, these estimates are also consistent with the observed age and metallicity derived for a large sample of dwarf galaxies

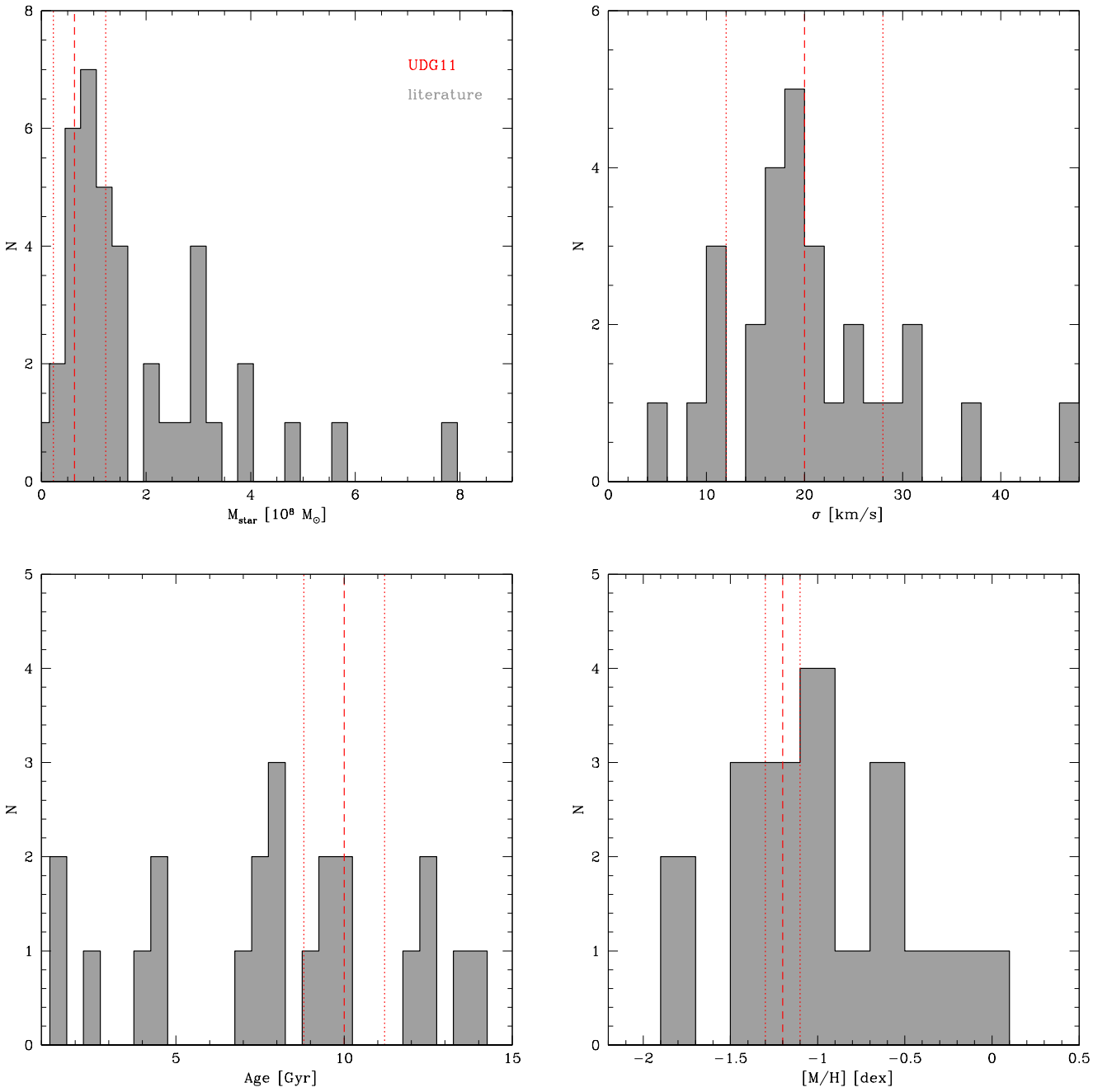

Fig. 12. Stellar kinematics and stellar populations for UDGs from the literature compared with UDG11. Histograms (in grey) represent the stellar mass (top-left), velocity dispersion (top-right), age (bottom-left), and metallicity (bottom-right) for UDGs from previous works (Ruiz-Lara et al. 2018; Ferré-Mateu et al. 2018; Chilingarian et al. 2019; van Dokkum et al. 2019; Emsellem et al. 2019; Fensch et al. 2019; Gannon et al. 2021, 2023; Toloba et al. 2018; Martín-Navarro et al. 2019). In all panels, the average value derived for UDG11 and error estimates are marked with the vertical red dashed and dotted lines, respectively. Values are obtained from the fit of the stacked spectrum inside $1R_e$, and are listed in the first column of Table 2.

(Heesters et al. 2023; Romero-Gómez et al. 2023), where ages and metallicities range from 5 to 14 Gyr, and from 0 to −1.9 dex, respectively.

A detailed discussion on the formation history of UDG11 is out of the scope of this paper, and will instead be presented in the context of the full sample. However, we briefly comment below on how the LEWIS data can be used to address the structure and formation of UDGs in a cluster environment. According to Sales et al. (2020), at a given stellar mass, the T-UDGs show lower velocity dispersion and higher metallicity than the B-UDGs and normal dwarf galaxies. In addition, B-UDGs are found at larger cluster-centric distances ($\geq 0.5R_{200}$) than T-UDGs, whose spatial distribution peaks around the cluster core (see Fig. 7 in Sales et al. 2020). The observed properties of UDG11, from the deep VST images and LEWIS data, are similar to those predicted for the B-UDGs. UDG11 is located on the west side of the cluster, at about $0.4R_{vir}$, in the low-density region of dwarf galaxies (see La Marca et al. 2022a), and the measured velocity dispersion and metallicity are similar to those of dwarf galaxies (see Fig. 13).

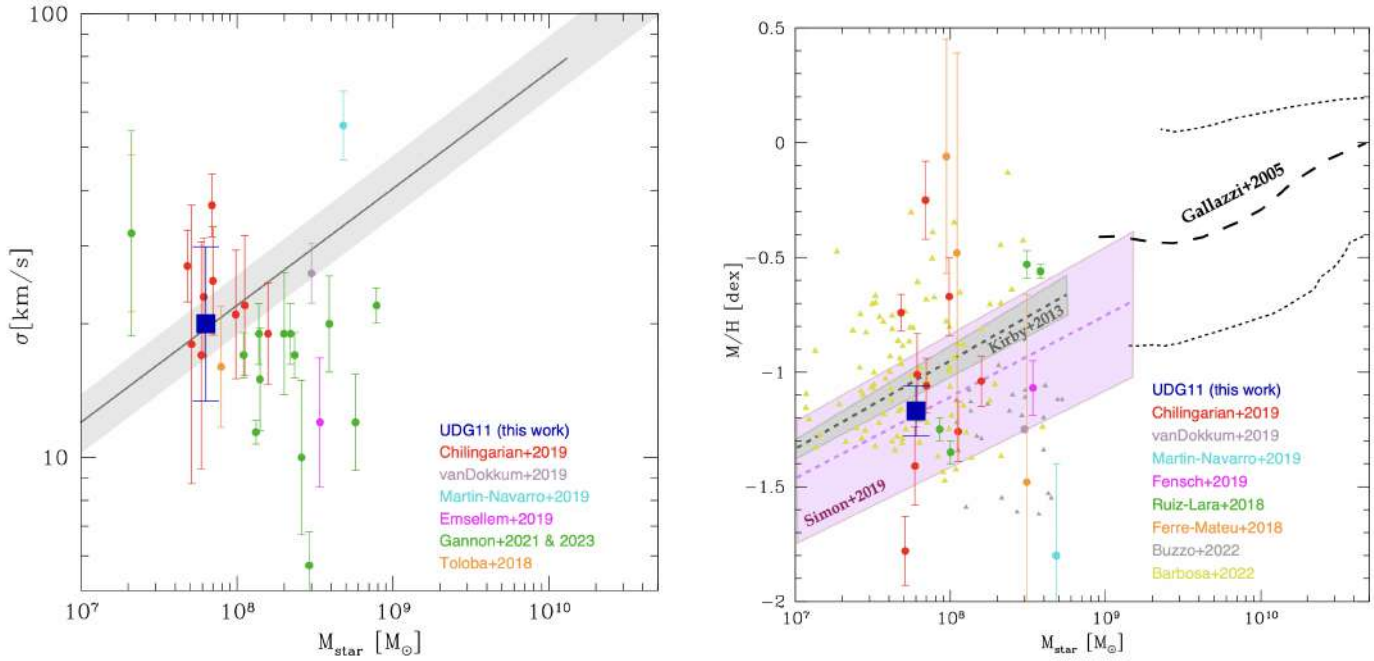

Fig. 13. Velocity dispersion and metallicity as a function of stellar mass for UDGs. Left panel: σ–mass relation for UDGs from the literature (coloured points) and UDG11 (blue square). The grey area corresponds to the observed baryonic Tully-Fisher relation (McGaugh 2012) obtained by scaling the rotation velocity by $\sqrt{3}$. Right panel: mass–metallicity relation from observations, including UDG11. The mass–metallicity relations found for dwarf galaxies by Kirby et al. (2013) and by Simon (2019) are marked in grey and purple regions, respectively. The average mass–metallicity relation for bright galaxies is marked by the black dashed line, and its range is shown by the two dotted lines (Gallazzi et al. 2005). The metallicities derived by fitting the spectral energy distribution by Buzzo et al. (2022) and Barbosa et al. (2020) are marked with grey and yellow triangles, respectively. In both panels, data points from Chilingarian et al. (2019) are UDG-like, because only two objects of the sample have $\mu_0 \geq 24$ mag arcsec^{-2} and $R_e \geq 1.5$ kpc.

6.2. Dark-matter content of UDG11

We computed the dynamical mass of UDG11 using the mass estimator proposed by Wolf et al. (2010), where $M_{1/2} = 4 \times R_e G^{-1} \langle\sigma\rangle_e^2$. Using $\langle\sigma\rangle_e = 20 \pm 8\,\mathrm{km\,s^{-1}}$, which was derived from the fit of the 1D stacked spectrum, we obtain $M_{1/2} = 4.2 \pm 0.8 \times 10^8\,M_\odot$. This is the dynamical mass inside half of the total luminosity. The absolute magnitude in the V band for UDG11 is $M_{V,0} = -14.6 \pm 0.7$ mag, and therefore the total dynamical mass-to-light ratio is $M/L_V = 2 \times M_{1/2}/L_V \simeq 14\,M_\odot/L_\odot$.

UDG11 seems to have a total mass comparable to Local Group dwarfs of similar luminosity, which show $M/L_V \sim 10-100$ (Battaglia & Nipoti 2022). This suggests a dwarf-like DM halo for this UDG.

According to the stellar mass–halo mass relation derived down to the lowest stellar masses (Wang et al. 2021), which are comparable to the stellar mass of UDG11 ($M_* \sim 10^8\,M_\odot$), the expected halo mass is $M_h \sim 10^{10}\,M_\odot$. A similar value is also obtained when using the halo mass–stellar mass relation derived by Zaritsky & Behroozi (2023), where $M_h = 10^{10.35} \times [M_*/(10^8\,M_\odot)]^{0.63} \simeq 1.7 \times 10^{10}\,M_\odot$.

Using the scaling relation between the halo mass and the total number of GCs, which is $\log[M_h] = 9.68 + 1.01 \times \log[N_{GC}]$ (Burkert & Forbes 2020), and assuming this it is still valid in the low-mass regime, a consistent value of halo mass is found of $M_h \sim 4 \times 10^{10}\,M_\odot$, where we adopt $N_{GC} = 5.9^{+2.2}_{-1.8}$ (see Sect. 5.5). However, it is worth noting here that this estimate for the halo mass is made under the assumption that the central GC1 is a nuclear star cluster, and that GC2 does not belong to UDG11. Including both GCs would result in a higher S_N and halo mass, which would still be consistent within the uncertainties with the values quoted in Sect. 5.5.

7. Summary and concluding remarks

In this paper, we present the LEWIS project. LEWIS is a large observing programme that began in 2021, the aim of which is to obtain the first homogeneous integral-field spectroscopic survey of LSB galaxies – including UDGs – in the Hydra I cluster of galaxies with MUSE at ESO-VLT. The LEWIS sample consists of 30 galaxies, that is, 22 UDGs and 8 LSB dwarfs, with effective surface brightnesses in the range $25 \leq \mu_e \leq 27.5$ mag arcsec^{-2} in the g band (Table 1). The total integration time per target varies from 2 h for the brightest objects up to 6 h for the faintest ones.

With the LEWIS project we expect to constrain *(i)* the fraction of baryonic versus DM content, *(ii)* the star formation history, and *(iii)* the GC content by means of spectroscopic S_N, in all sample galaxies. Given the large variety of observed properties for UDGs (mainly based on deep images), and theoretical scenarios, which envisage various possibilities for the formation of this kind of galaxy, the main outcomes of this project are a notable boost to our knowledge of UDG structure and formation.

LEWIS observations are still ongoing. In this paper, we present the LEWIS sample and the measured redshift for the 20 targets (16 UDGs and 4 LSB dwarfs) observed so far. We confirm 14 of these as Hydra I cluster members, with systemic velocities ranging from 3483 km s^{-1} to 4302 km s^{-1}, which correspond to $\sim 1\sigma$ from the cluster mean velocity ($V_{sys} = 3683 \pm 46\,\mathrm{km\,s^{-1}}$, $\sigma_{cluster} \sim 700\,\mathrm{km\,s^{-1}}$). Three galaxies of the sample have systemic velocities within $2\sigma_{cluster}$, and therefore may still be considered as cluster members. Finally, the remaining three galaxies with larger or smaller systemic velocities could be considered as background or foreground galaxies, respectively.

To assess the quality of the LEWIS data, we also describe the data analysis that we adopt in this project for one of the sample galaxies, UDG11, which was chosen as a test case. UDG11 is located far from the cluster core, on the western side at a distance of $\sim 0.4 R_{\rm vir}$. It has an absolute r-band magnitude of $M_r = -14.75$ mag and a stellar mass of $0.63 \times 10^8\, M_\odot$. The MUSE data obtained for this target have a total integration time of 6.10 h, which allowed us to obtain a $S/N \sim 16$ per spaxel for the 1D stacked spectrum inside $1R_{\rm e}$. For this target, we derived the stellar kinematics, constrained the average age and metallicity of the stellar populations, estimated the total number of spectroscopically confirmed GCs, and provided the dynamical mass. All the above quantities are compared with the available measurements for UDGs and dwarf galaxies in the literature. Our results are summarised below.

- By fitting the stacked spectrum inside $1R_{\rm e}$ on the full MUSE rest-frame wavelength range (4800−9000 Å), we obtained a velocity dispersion of $\sigma = 20 \pm 8\,{\rm km\,s^{-1}}$, a metallicity of $[M/{\rm H}] = -1.17 \pm 0.11$ dex, and an age of 10 ± 1 Gyr.
- The spatially resolved stellar kinematics obtained from the Voronoi-binned spectra with $S/N = 10$ indicates that UDG11 does not show a significant gradient of $V_{\rm sys}$ or $\sigma_{\rm LOS}$ along its major and minor photometric axes. The mean value of the velocity dispersion is $\langle\sigma\rangle_{\rm e} = 27 \pm 8\,{\rm km\,s^{-1}}$, which is consistent with the estimate from the fit of the stacked spectrum inside $1R_{\rm e}$.
- The absence of emission lines in the MUSE cube for UDG11 suggests that this galaxy lacks ionised gas.
- Four point sources in the UDG11 cube have radial velocities consistent with the Hydra I cluster. Two of those four sources appear kinematically associated to UDG11 (with relative velocities of ∼10–30 km s^{-1}). The other two sources, with larger velocities, are classified as intra-cluster GCs. When corrected for our spectroscopic measurement magnitude limit, we obtain an estimated total number of GCs of $N_{\rm GC} = 5.9^{+2.2}_{-1.8}$, and the corresponding specific frequency is $S_N = 8.4^{+3.2}_{-2.7}$. This is consistent with the typical S_N estimates for dwarf galaxies of similar luminosity (Lim et al. 2018).
- The stellar velocity dispersion, age, and metallicity derived for UDG11 are comparable with values derived for other UDGs of similar stellar mass estimated in previous works (see Fig. 12).
- The total mass inside $1R_{\rm e}$ and the total dynamical mass-to-light ratio estimated for UDG11 are $M_{1/2} \simeq 4 \times 10^8\, M_\odot$ and $M/L_V \simeq 14 M_\odot/L_\odot$, respectively. These estimates are comparable to those of Local Group dwarfs of similar total luminosity (Battaglia & Nipoti 2022), suggesting a dwarf-like DM halo for this UDG.

In summary, we find that UDG11 is old and metal poor, and has a DM content comparable to those observed for dwarf galaxies. As this UDG is also gas poor, all these observed properties might suggest that UDG11 was formed in response to the action of an external process, and that formation channels based on internal mechanisms can be reasonably excluded (see Sect. 1 and Fig. 1). In particular, UDG11 might have formed as a LSB, which then lost its gas and was quenched when it was accreted by the Hydra I cluster.

These results further demonstrate the power of IF spectroscopic data, and in particular of the MUSE at ESO-VLT, in studying the structure of LSB galaxies and in constraining the formation history of UDGs. To date, similar studies are available for only about 35 UDGs in total, mainly in the Coma cluster, which is probably because of the challenging observations at such very low surface brightness levels. In particular, IF spectroscopy is only available for a dozen UDGs (Emsellem et al. 2019; Müller et al. 2020; Gannon et al. 2021, 2023). With LEWIS we will make a decisive impact in this field: we will double the number of spectroscopically studied UDGs and establish the properties of a (nearly) complete sample of UDGs in a galaxy cluster, Hydra I. This cluster is currently undergoing a phase of active assembly, thus offering a range of environments for its members.

Acknowledgements. Based on observations collected at the European Southern Observatory under ESO programmes 108.222P.001, 108.222P.002, 108.222P.003. We thank the anonymous referee for their useful suggestions that helped to improve the paper. Authors wish to thank Dr. Lodovico Coccato (ESO-Garching) for the kind support during the MUSE data reduction. E.I. wish to thank L. Buzzo, P.-A. Duc, A. Ferre-Mateu, J. Gannon, F. Marleau, O. Muller and R. Peletier for the useful comments and discussions on the work presented in this paper. E.I. acknowledges support by the INAF GO funding grant 2022-2023. JH wishes to acknowledge CSC – IT Center for Science, Finland, for computational resources. EMC is supported by MIUR grant PRIN 2017 20173ML3WW-001 and Padua University grants DOR2019-2021. J. F-B acknowledges support through the RAVET project by the grant PID2019-107427GB-C32 from the Spanish Ministry of Science, Innovation and Universities (MCIU), and through the IAC project TRACES which is partially supported through the state budget and the regional budget of the Consejería de Economía, Industria, Comercio y Conocimiento of the Canary Islands Autonomous Community. MAR acknowledges funding from the European Union's Horizon 2020 research and innovation programme under the Marie Skłodowska-Curie grant agreement No 101066353 (project ELATE). K.F. acknowledges support through the ESA Research Fellowship programme. Authors acknowledge the use of the *dfitspy* tool (Thomas 2019) and MUSE Python Data Analysis Framework (MPDAF) (Bacon et al. 2016).

References

Amorisco, N. C., & Loeb, A. 2016, MNRAS, 459, L51
Arnaboldi, M., Ventimiglia, G., Iodice, E., Gerhard, O., & Coccato, L. 2012, A&A, 545, A37
Bacon, R., Piqueras, L., Conseil, S., Richard, J., & Shepherd, M. 2016, MPDAF: MUSE Python Data Analysis Framework, Astrophysics Source Code Library [record ascl:1611.003]
Bacon, R., Conseil, S., Mary, D., et al. 2017, A&A, 608, A1
Barbosa, C. E., Arnaboldi, M., Coccato, L., et al. 2018, A&A, 609, A78
Barbosa, C. E., Zaritsky, D., Donnerstein, R., et al. 2020, ApJS, 247, 46
Barbosa, C. E., Spiniello, C., Arnaboldi, M., et al. 2021, A&A, 649, A93
Battaglia, G., & Nipoti, C. 2022, Nat. Astron., 6, 1492
Benavides, J. A., Sales, L. V., Abadi, M. G., et al. 2021, Nat. Astron., 5, 1255
Bennet, P., Sand, D. J., Zaritsky, D., et al. 2018, ApJ, 866, L11
Bittner, A., Falcón-Barroso, J., Nedelchev, B., et al. 2019, A&A, 628, A117
Bothun, G. D., Impey, C. D., & Malin, D. F. 1991, ApJ, 376, 404
Bradley, L., Sipőcz, B., Robitaille, T., et al. 2020, https://zenodo.org/records/4044744
Burkert, A., & Forbes, D. A. 2020, AJ, 159, 56
Buzzo, M. L., Forbes, D. A., Brodie, J. P., et al. 2022, MNRAS, 517, 2231
Cappellari, M. 2017, MNRAS, 466, 798
Cappellari, M., & Copin, Y. 2003, MNRAS, 342, 345
Cappellari, M., & Emsellem, E. 2004, PASP, 116, 138
Carleton, T., Guo, Y., Munshi, F., Tremmel, M., & Wright, A. 2021, MNRAS, 502, 398
Cenarro, A. J., Cardiel, N., Gorgas, J., et al. 2001, MNRAS, 326, 959
Chilingarian, I. V., Afanasiev, A. V., Grishin, K. A., Fabricant, D., & Moran, S. 2019, ApJ, 884, 79
Christlein, D., & Zabludoff, A. I. 2003, ApJ, 591, 764
Collins, M. L. M., Read, J. I., Ibata, R. A., et al. 2021, MNRAS, 505, 5686
Conselice, C. J. 2018, Res. Notes Am. Astron. Soc., 2, 43
Di Cintio, A., Brook, C. B., Dutton, A. A., et al. 2017, MNRAS, 466, L1
Duc, P.-A., Paudel, S., McDermid, R. M., et al. 2014, MNRAS, 440, 1458
Eftekhari, F. S., Peletier, R. F., Scott, N., et al. 2022, MNRAS, 517, 4714
Emsellem, E., van der Burg, R. F. J., Fensch, J., et al. 2019, A&A, 625, A76
Fahrion, K., Lyubenova, M., Hilker, M., et al. 2020, A&A, 637, A26
Falcón-Barroso, J., Sánchez-Blázquez, P., Vazdekis, A., et al. 2011, A&A, 532, A95
Fensch, J., van der Burg, R. F. J., Jeřábková, T., et al. 2019, A&A, 625, A77
Ferguson, H. C., & Sandage, A. 1988, AJ, 96, 1520
Ferré-Mateu, A., Alabi, A., Forbes, D. A., et al. 2018, MNRAS, 479, 4891

Forbes, D. A., Gannon, J. S., Romanowsky, A. J., et al. 2021, MNRAS, 500, 1279
Forbes, D. A., Gannon, J., Iodice, E., et al. 2023, MNRAS, 525, L93
Freudling, W., Romaniello, M., Bramich, D. M., et al. 2013, A&A, 559, A96
Gadotti, D. A., & de Souza, R. E. 2005, ApJ, 629, 797
Gallazzi, A., Charlot, S., Brinchmann, J., White, S. D. M., & Tremonti, C. A. 2005, MNRAS, 362, 41
Gannon, J. S., Dullo, B. T., Forbes, D. A., et al. 2021, MNRAS, 502, 3144
Gannon, J. S., Forbes, D. A., Brodie, J. P., et al. 2023, MNRAS, 518, 3653
Georgiev, I. Y., Puzia, T. H., Goudfrooij, P., & Hilker, M. 2010, MNRAS, 406, 1967
Gerhard, O. E. 1993, MNRAS, 265, 213
Girardi, M., Borgani, S., Giuricin, G., Mardirossian, F., & Mezzetti, M. 1998, ApJ, 506, 45
Girardi, L., Bressan, A., Bertelli, G., & Chiosi, C. 2000, A&AS, 141, 371
Gu, M., Conroy, C., Law, D., et al. 2018, ApJ, 859, 37
Harris, W. E., & van den Bergh, S. 1981, AJ, 86, 1627
Heesters, N., Müller, O., Marleau, F. R., et al. 2023, A&A, 676, A33
Hilker, M., Richtler, T., Barbosa, C. E., et al. 2018, A&A, 619, A70
Impey, C., Bothun, G., & Malin, D. 1988, ApJ, 330, 634
Iodice, E., Cantiello, M., Hilker, M., et al. 2020, A&A, 642, A48
Iodice, E., La Marca, A., Hilker, M., et al. 2021, A&A, 652, L11
Janssens, S. R., Abraham, R., Brodie, J., Forbes, D. A., & Romanowsky, A. J. 2019, ApJ, 887, 92
Kirby, E. N., Cohen, J. G., Guhathakurta, P., et al. 2013, ApJ, 779, 102
Koda, J., Yagi, M., Yamanoi, H., & Komiyama, Y. 2015, ApJ, 807, L2
Kroupa, P. 2001, MNRAS, 322, 231
La Marca, A., Iodice, E., Cantiello, M., et al. 2022a, A&A, 665, A105
La Marca, A., Peletier, R., Iodice, E., et al. 2022b, A&A, 659, A92
Leisman, L., Haynes, M. P., Janowiecki, S., et al. 2017, ApJ, 842, 133
Lelli, F., Duc, P.-A., Brinks, E., et al. 2015, A&A, 584, A113
Lim, S., Peng, E. W., Côté, P., et al. 2018, ApJ, 862, 82
Lim, S., Côté, P., Peng, E. W., et al. 2020, ApJ, 899, 69
Lima-Dias, C., Monachesi, A., Torres-Flores, S., et al. 2021, MNRAS, 500, 1323
Mancera Piña, P. E., Aguerri, J. A. L., Peletier, R. F., et al. 2019, MNRAS, 485, 1036
Marleau, F. R., Habas, R., Poulain, M., et al. 2021, A&A, 654, A105
Martín-Navarro, I., Romanowsky, A. J., Brodie, J. P., et al. 2019, MNRAS, 484, 3425
McGaugh, S. S. 2012, AJ, 143, 40
Miller, C. J., Stark, A., Gifford, D., & Kern, N. 2016, ApJ, 822, 41
Misgeld, I., Mieske, S., & Hilker, M. 2008, A&A, 486, 697
Misgeld, I., Mieske, S., Hilker, M., et al. 2011, A&A, 531, A4
Müller, O., Rich, R. M., Román, J., et al. 2019, A&A, 624, L6
Müller, O., Marleau, F. R., Duc, P.-A., et al. 2020, A&A, 640, A106
Pandya, V., Romanowsky, A. J., Laine, S., et al. 2018, ApJ, 858, 29
Ploeckinger, S., Sharma, K., Schaye, J., et al. 2018, MNRAS, 474, 580
Poggianti, B. M., Gullieuszik, M., Tonnesen, S., et al. 2019, MNRAS, 482, 4466
Prole, D. J., Hilker, M., van der Burg, R. F. J., et al. 2019a, MNRAS, 484, 4865
Prole, D. J., van der Burg, R. F. J., Hilker, M., & Davies, J. I. 2019b, MNRAS, 488, 2143
Richter, O. G. 1987, A&AS, 67, 237
Richter, O. G., Materne, J., & Huchtmeier, W. K. 1982, A&A, 111, 193
Richtler, T., Salinas, R., Misgeld, I., et al. 2011, A&A, 531, A119
Román, J., & Trujillo, I. 2017, MNRAS, 468, 703
Román, J., Beasley, M. A., Ruiz-Lara, T., & Valls-Gabaud, D. 2019, MNRAS, 486, 823
Romero-Gómez, J., Peletier, R. F., Aguerri, J. A. L., et al. 2023, MNRAS, 522, 130
Rong, Y., Guo, Q., Gao, L., et al. 2017, MNRAS, 470, 4231
Ruiz-Lara, T., Beasley, M. A., Falcón-Barroso, J., et al. 2018, MNRAS, 478, 2034
Saifollahi, T., Trujillo, I., Beasley, M. A., Peletier, R. F., & Knapen, J. H. 2021, MNRAS, 502, 5921
Saifollahi, T., Zaritsky, D., Trujillo, I., et al. 2022, MNRAS, 511, 4633
Sales, L. V., Navarro, J. F., Peñafiel, L., et al. 2020, MNRAS, 494, 1848
Sandage, A., & Binggeli, B. 1984, AJ, 89, 919
Sarzi, M., Iodice, E., Coccato, L., et al. 2018, A&A, 616, A121
Schlegel, D. J., Finkbeiner, D. P., & Davis, M. 1998, ApJ, 500, 525
Shin, E.-J., Jung, M., Kwon, G., et al. 2020, ApJ, 899, 25
Silk, J. 2019, MNRAS, 488, L24
Simon, J. D. 2019, ARA&A, 57, 375
Soto, K. T., Lilly, S. J., Bacon, R., Richard, J., & Conseil, S. 2016, MNRAS, 458, 3210
Thomas, R. 2019, J. Open Source Soft., 4, 1249
Toloba, E., Lim, S., Peng, E., et al. 2018, ApJ, 856, L31
Tremmel, M. J., Wright, A., Munshi, F., et al. 2019, Am. Astron. Soc. Meeting Abstr., 233, 416.04
Tremmel, M., Wright, A. C., Brooks, A. M., et al. 2020, MNRAS, 497, 2786
Trujillo, I., Roman, J., Filho, M., & Sánchez Almeida, J. 2017, ApJ, 836, 191
van der Burg, R. F. J., Hoekstra, H., Muzzin, A., et al. 2017, A&A, 607, A79
van der Marel, R. P., & Franx, M. 1993, ApJ, 407, 525
van Dokkum, P. G., Romanowsky, A. J., Abraham, R., et al. 2015, ApJ, 804, L26
van Dokkum, P., Abraham, R., Romanowsky, A. J., et al. 2017, ApJ, 844, L11
van Dokkum, P., Danieli, S., Cohen, Y., et al. 2018, Nature, 555, 629
van Dokkum, P., Wasserman, A., Danieli, S., et al. 2019, ApJ, 880, 91
van Dokkum, P., Shen, Z., Keim, M. A., et al. 2022, Nature, 605, 435
Vazdekis, A., Casuso, E., Peletier, R. F., & Beckman, J. E. 1996, ApJS, 106, 307
Vazdekis, A., Sánchez-Blázquez, P., Falcón-Barroso, J., et al. 2010, MNRAS, 404, 1639
Vazdekis, A., Ricciardelli, E., Cenarro, A. J., et al. 2012, MNRAS, 424, 157
Vazdekis, A., Coelho, P., Cassisi, S., et al. 2015, MNRAS, 449, 1177
Vazdekis, A., Koleva, M., Ricciardelli, E., Röck, B., & Falcón-Barroso, J. 2016, MNRAS, 463, 3409
Venhola, A., Peletier, R., Laurikainen, E., et al. 2017, A&A, 608, A142
Villegas, D., Jordán, A., Peng, E. W., et al. 2010, ApJ, 717, 603
Wang, Y., Nadler, E. O., Mao, Y.-Y., et al. 2021, ApJ, 915, 116
Webb, K. A., Villaume, A., Laine, S., et al. 2022, MNRAS, 516, 3318
Wegner, G. A., Corsini, E. M., Thomas, J., et al. 2012, AJ, 144, 78
Weilbacher, P. M., Streicher, O., & Palsa, R. 2016, Astrophysics Source Code Library [record ascl:1610.004]
Weilbacher, P. M., Palsa, R., Streicher, O., et al. 2020, A&A, 641, A28
Wolf, J., Martinez, G. D., Bullock, J. S., et al. 2010, MNRAS, 406, 1220
Yagi, M., Koda, J., Komiyama, Y., & Yamanoi, H. 2016, ApJS, 225, 11
Yozin, C., & Bekki, K. 2015, MNRAS, 452, 937
Zaritsky, D., & Behroozi, P. 2023, MNRAS, 519, 871
Zaritsky, D., Donnerstein, R., Karunakaran, A., et al. 2022, ApJS, 261, 11
Zoutendijk, S. L., Brinchmann, J., Boogaard, L. A., et al. 2020, A&A, 635, A107

[1] INAF – Astronomical Observatory of Capodimonte, Salita Moiariello 16, 80131 Naples, Italy
e-mail: enrichetta.iodice@inaf.it
[2] European Southern Observatory, Karl-Schwarzschild-Strasse 2, 85748 Garching bei München, Germany
[3] University of Naples "Federico II", C.U. Monte Sant'Angelo, Via Cinthia, 80126 Naples, Italy
[4] INAF – Astronomical Observatory of Abruzzo, Via Maggini, 64100 Teramo, Italy
[5] Gran Sasso Science Institute, viale Francesco Crispi 7, 67100 L'Aquila, Italy
[6] Finnish Centre for Astronomy with ESO (FINCA), Quantum, Vesilinnantie 5, 20014 University of Turku, Finland
[7] Tuorla Observatory, Department of Physics and Astronomy, Quantum, Vesilinnantie 5, 20014 University of Turku, Finland
[8] European Southern Observatory, Alonso de Cordova 3107, Vitacura, Santiago, Chile
[9] Cambridge Astronomy Survey Unit (CASU), Institute of Astronomy, University of Cambridge, Madingley Road, Cambridge CB3 0HA, UK
[10] Centre for Astrophysics & Supercomputing, Swinburne University of Technology, John st., Hawthorn, VIC 3122, Australia
[11] INAF – Osservatorio Astronomico di Padova, Vicolo dell'Osservatorio 5, 35122 Padova, Italy
[12] Department of Physics, University of Oxford, Denys Wilkinson Building, Keble Road, Oxford OX1 3RH, UK
[13] Dipartimento di Fisica e Astronomia "G. Galilei", Università di Padova, vicolo dell'Osservatorio 3, 35122 Padova, Italy
[14] Instituto de Astrofísica de Canarias, Calle Vía Láctea s/n, 38200 La Laguna, Spain
[15] European Space Agency (ESA), European Space Exploration and Research Centre (ESTEC), Keplerlaan 1, 2201 AZ Noordwijk, The Netherlands
[16] Instituto de Radioastronomía y Astrofísica, UNAM, Campus Morelia, A.P. 3-72, México C.P. 58089, Mexico
[17] Kapteyn Astronomical Institute, University of Groningen, Postbus 800, 9700 AV Groningen, The Netherlands
[18] SRON Netherlands Institute for Space Research, Landleven 12, 9747 AD Groningen, The Netherlands
[19] Armagh Observatory and Planetarium, College Hill, Armagh BT61 9DG, UK

Appendix A: MUSE reconstructed images and stacked spectra

In this section, for each target observed in the LEWIS sample (see Table1), we show the reconstructed images from the MUSE cube and the stacked spectrum inside $1R_e$, including the best fit to derive the redshift estimate. All of these images were obtained using the standard data-reduction pipeline with some optimised parameters, as described in Sect. 3.2.

Appendix B: Error estimates: General overview

The uncertainties present in the analysis are related to the following sources of error:

1. Quality of the data (noise and residual sky lines).
1. Uncertainty on the spectral resolution.
2. Prior on the regularisation.
3. Choice of spectral mask.
4. Calibration errors and selection of multiplicative and additive polynomials.

Here we describe how we estimate the level of error from these sources of uncertainty:

1. Our MUSE spectrum for UDG11 has a per pixel SNR of 16. This significant amount of noise comes from two sources. The statistics of counting photons, which can be described with a Poissonian function, and a systematic source that includes uncorrected calibration problems, sky-line residuals, and other imperfections of the reduction pipeline. While the Poissonian noise is not usually a source of bias, systematic noise can often present severe bias effects if not properly addressed, as its effect on the spectrum can be easily confused as part of the signal.
   We treated most of the systematic effects using an improved datacube reduction pipeline (see Sec. 3.2) and proper masking of noisy and contaminated regions in the analysed spectra (see e.g., Fig. 5), improving the effective SNR to ∼20 per pixel. Therefore, we only benefit from an upper limit on possible biases. We give such an estimate using simulations in Sect. 5, and unless stated, we henceforth assume that most of the errors are dominated by Poisson statistics.
2. An estimate of the typical MUSE LSF was measured by Bacon et al. (2017) and Emsellem et al. (2019). We used the equation given by Bacon et al. (2017) to approximate the MUSE LSF under the assumption that at the best FWHM achieved by the data, the templates never significantly (ΔFWHM $>$ 0.1 Å) fall below the resolution of the MUSE spectra. From Bacon et al. (2017), we expect a maximum deviation from the true FWHM at any point of the wavelength axis of about ΔFWHM = 0.1 Å. This would translate to an uncertainty of $<$ 10 km/s as shown in Fig. 7.
3. Regularisation (stellar populations only): we used the suggested pPXF method to select a regularisation parameter depending on the data noise, which is tied to the SNR. In this sense, regularisation is not an independent source of uncertainty.
4. Choice of spectral mask: minor changes on the spectral mask selection can cause small variations on the resulting parameters, and therefore we change it randomly for our error estimation described in Appendix C.
5. Calibration errors: usually corrected using multiplicative and additive polynomials. A study of the effect of the additive polynomial degree for this particular source is presented in the main text of this paper (see Fig. 9). Regarding the effect of Legendre multiplicative polynomials, we ran several tests to address this effect. We verify that at degrees $8-11$ there are virtually no differences in the total metallicity and median age of the recovered stellar population, but the differences grow up to 0.1 dex in $[M/H]$ and 1 Gyr in stellar age when using a very low $(5-7)$ or high (>12) degree. We therefore place a strong prior on a Legendre multiplicative polynomial degree of 10. In summary, we find that when properly constrained, the above effects have a similar contribution to the total uncertainty.

Appendix C: Error bar estimation

C.1. Velocity dispersion

To determine the error bars on the systemic velocity and velocity dispersion of the $1R_e$ stacked spectrum, we decided to apply a bootstrap-like procedure: First, we generated different variations of the stacked spectrum by removing and replacing random regions (with spaxels surrounding $1R_e$) within the extraction zone. This corresponds to 10% of all stacked spaxels. Second, we refit the spectrum introducing Poissonian noise without drastically reducing the SNR. Effectively, we introduced Poissonian noise that introduces a standard deviation on the SNR per pixel distribution of <3. Finally, we fit the generated spectra via exploring a grid of randomly generated input parameters (described in Appendix B), emulating common Monte Carlo approaches. In all cases, we did not perturb the polynomial degrees used as described in Sect. 5.4. Our results show that the velocity dispersion measurement on the stacked spectrum has an uncertainty of 10 km/s, which agrees with our simulations (Appendix D).

C.2. Stellar population

To get age and metallicity uncertainties, we applied the same methodology as above but with the inclusion of mild perturbations on the regularisation parameter as a function of S/N, in addition to fixing the velocity dispersion values (within 1σ) to those obtained in the previous step.

Appendix D: Simulations

D.1. Signal-to-noise ratio limitations

As described in Sect. 5.1, from the best fit of the stacked spectrum inside $1R_e$ of UDG11 we obtained a velocity dispersion of $\sim$ 20 km/s, which is lower than the spectra resolution of MUSE. In addition, we aim to measure metallicities with uncertainties below $\sim$ 0.3. To achieve this, we require a clear understanding of the performance of pPXF and our pipeline in measuring small variations on the width of the main absorption lines with limited SNR. Therefore, based on the E-MILES models, we simulated mock UDG11-like spectra to study how the retrieved quantities from the pPXF fit vary with the SNR of the spectrum. Firstly, we took a stellar population with log(Age)=10 and $[M/H]= -1.2$, and constructed a synthetic spectrum based on it. Next, we convolved the spectrum with an approximated version of the MUSE LSF as presented in Bacon et al. (2017). Finally, we further convolved it with varying kernels to simulate different velocity dispersions. Subsequently, we introduced noise by generating several mock spectra with different S/N levels ranging from 5 to 120 per pixel by adding Poissonian noise. This allows us to evaluate the performance of the fit at very low S/N values. Figure 7 illustrates the results of this test. The figures show an unbiased trend that performs relatively well at S/N $\sim 10-15$ when trying

to retrieve velocity dispersion as low as $\sigma \sim 15$ km/s. The error at this level is of about 10 km/s.

D.2. Bias analysis

In order to put a rough upper bound on the maximum degree of bias in our results under the assumption that all of our noise is systematic, we extract a clean background region of the same size as the one used for the stacked 1D UDG11 spectrum present on the same cube. Then, we repeat the procedures described in Sect. D, including the background spectrum (containing residual sky lines and other systematics) instead of the random noise. After 1000 simulations, we estimate a maximum bias of around +0.1 in metallicity, and a negligible one on the mean stellar age.

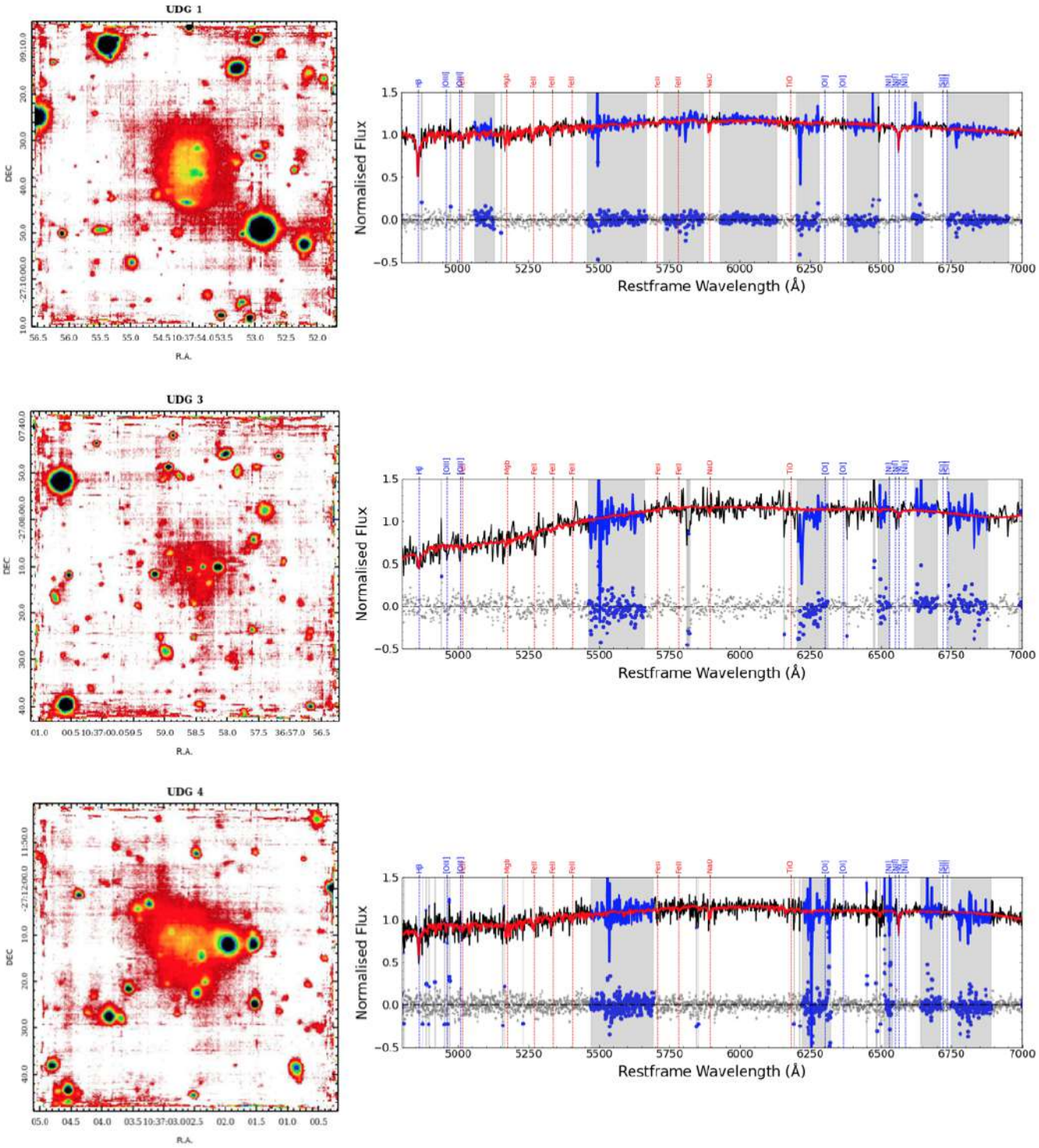

Fig. D.1. MUSE reconstructed images (left panels) and stacked spectra (right panels) of the observed LEWIS targets. From the top to lower panels, UDG1, UDG3, and UDG4 are shown, respectively. The red line corresponds to the pPXF best fit using the setup described in Sect. 4. Grey boxes mark the masked regions, which are excluded from the fit.

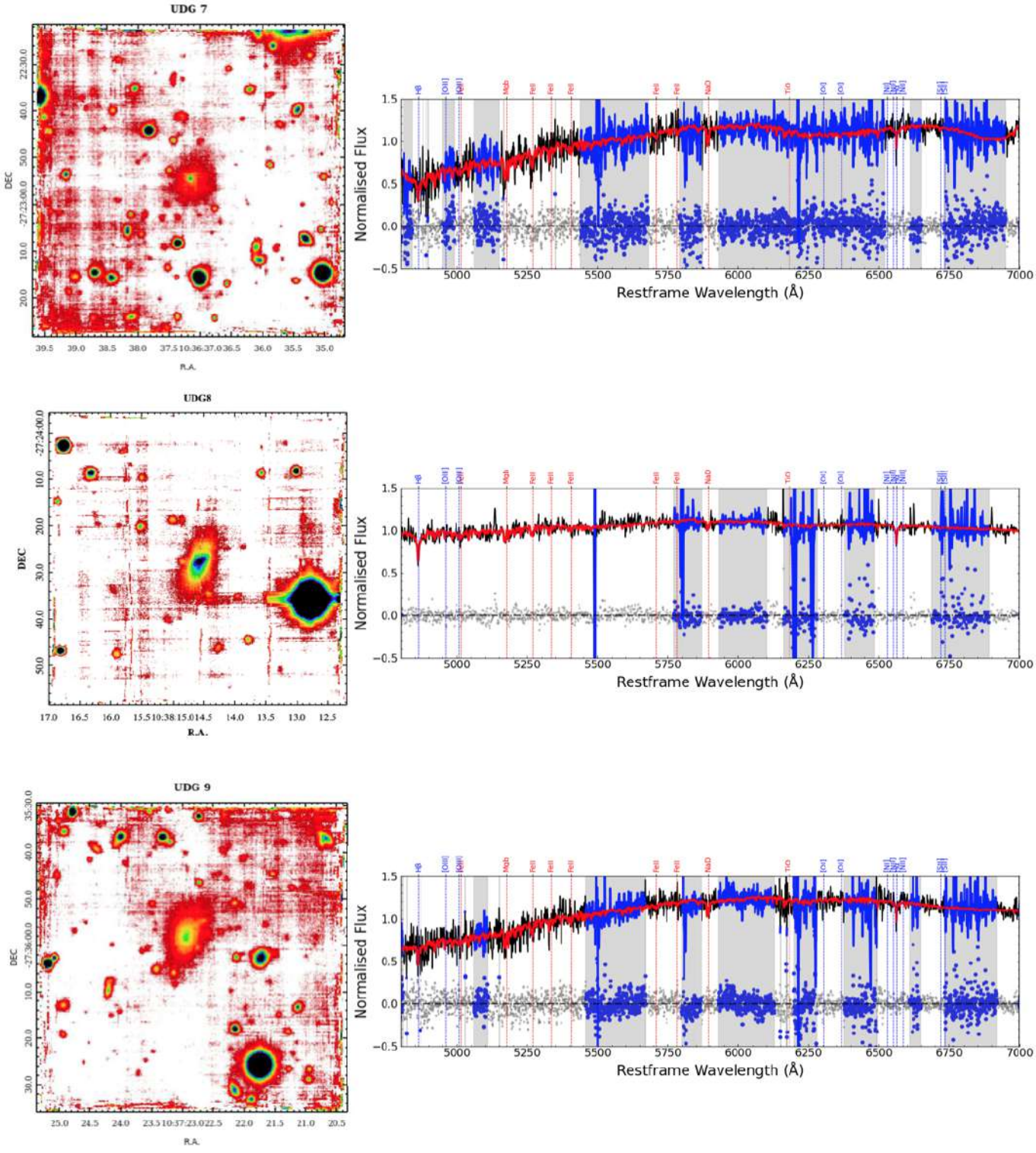

Fig. D.2. Same as Fig. D.1, but for UDG7, UDG8, and UDG9.

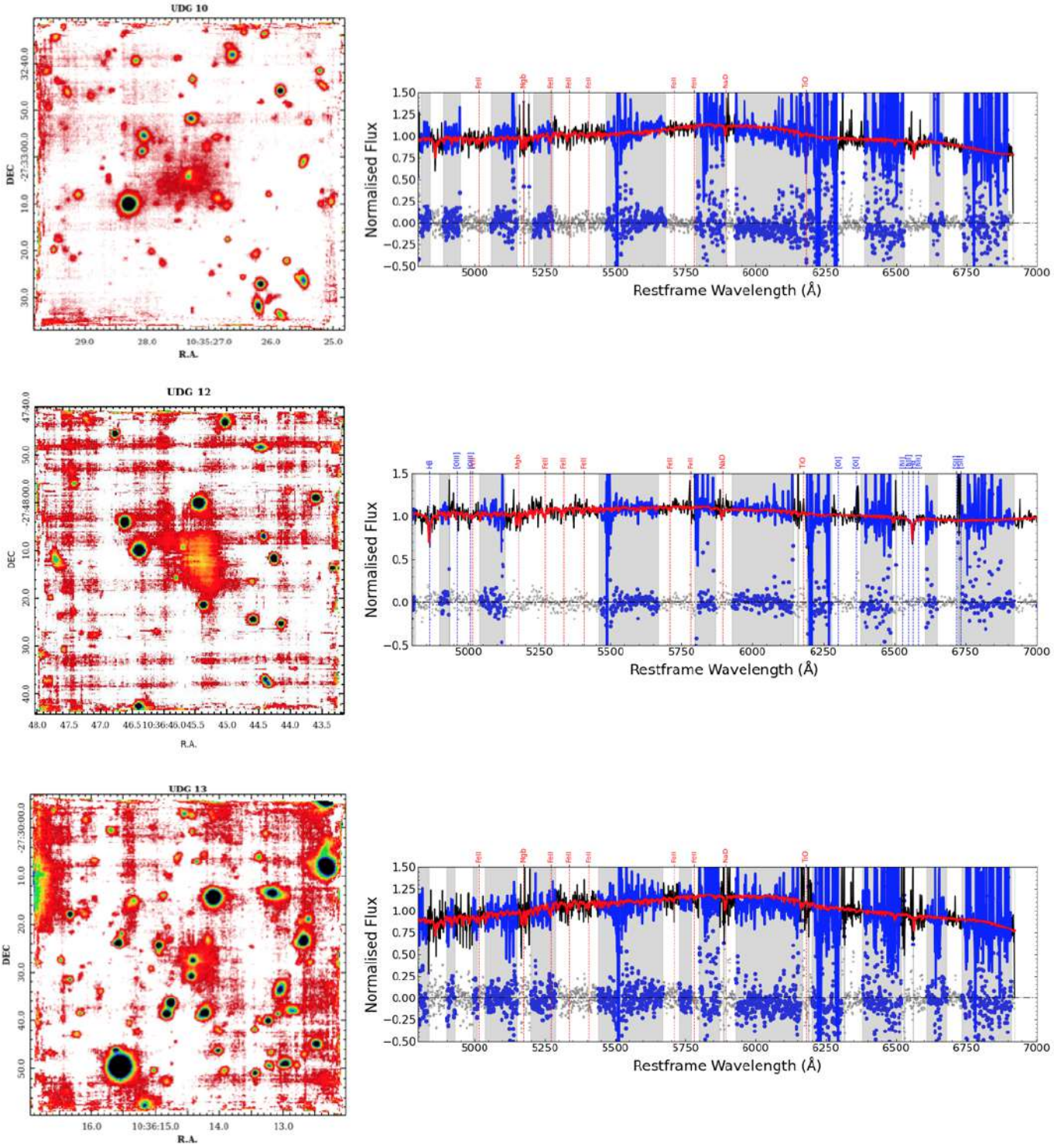

Fig. D.3. Same as Fig. D.1, but for UDG10, UDG12, and UDG13.

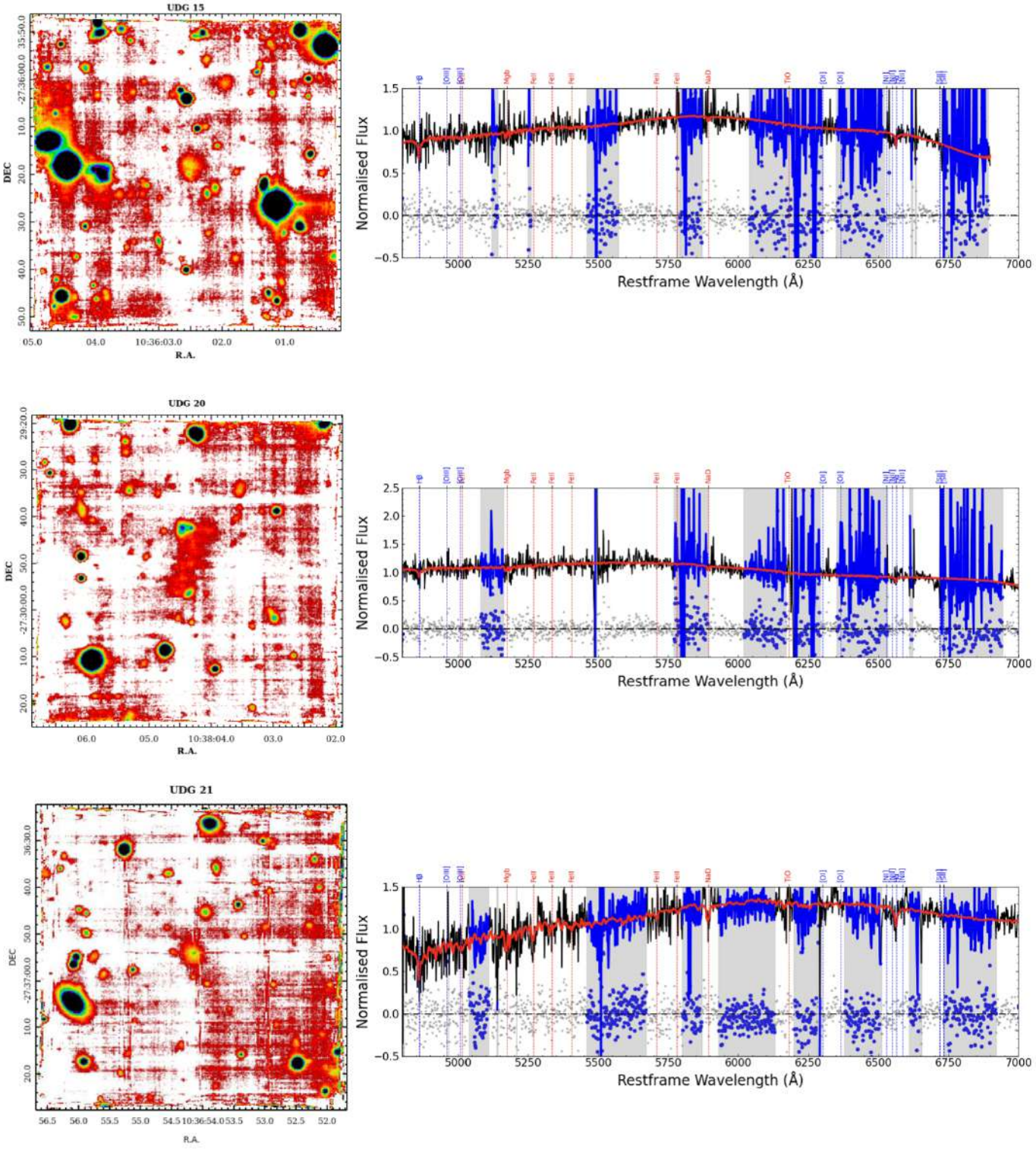

Fig. D.4. Same as Fig. D.1, but for UDG15, UDG20, and UDG21.

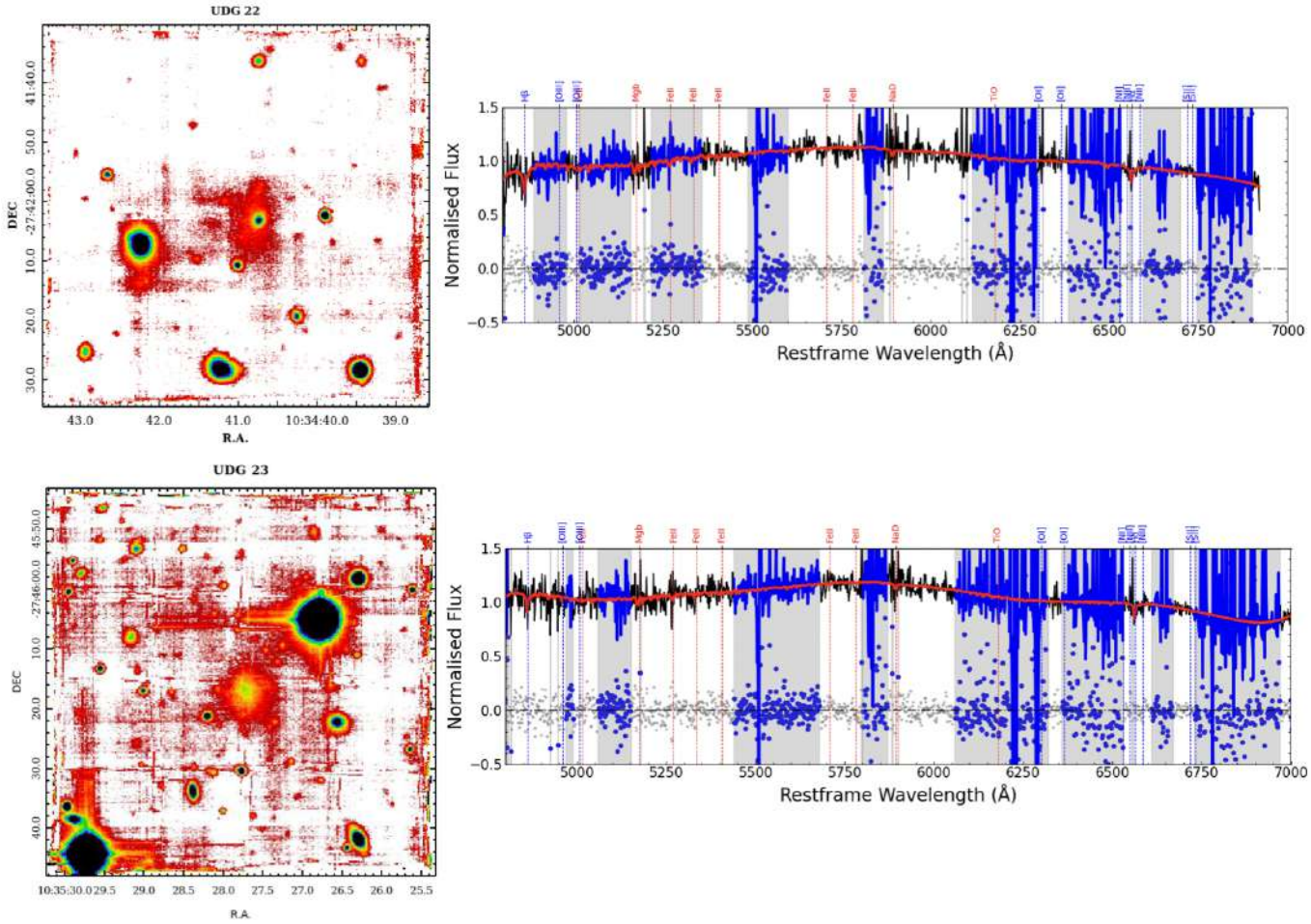

Fig. D.5. Same as Fig. D.1, but for UDG22 and UDG23.

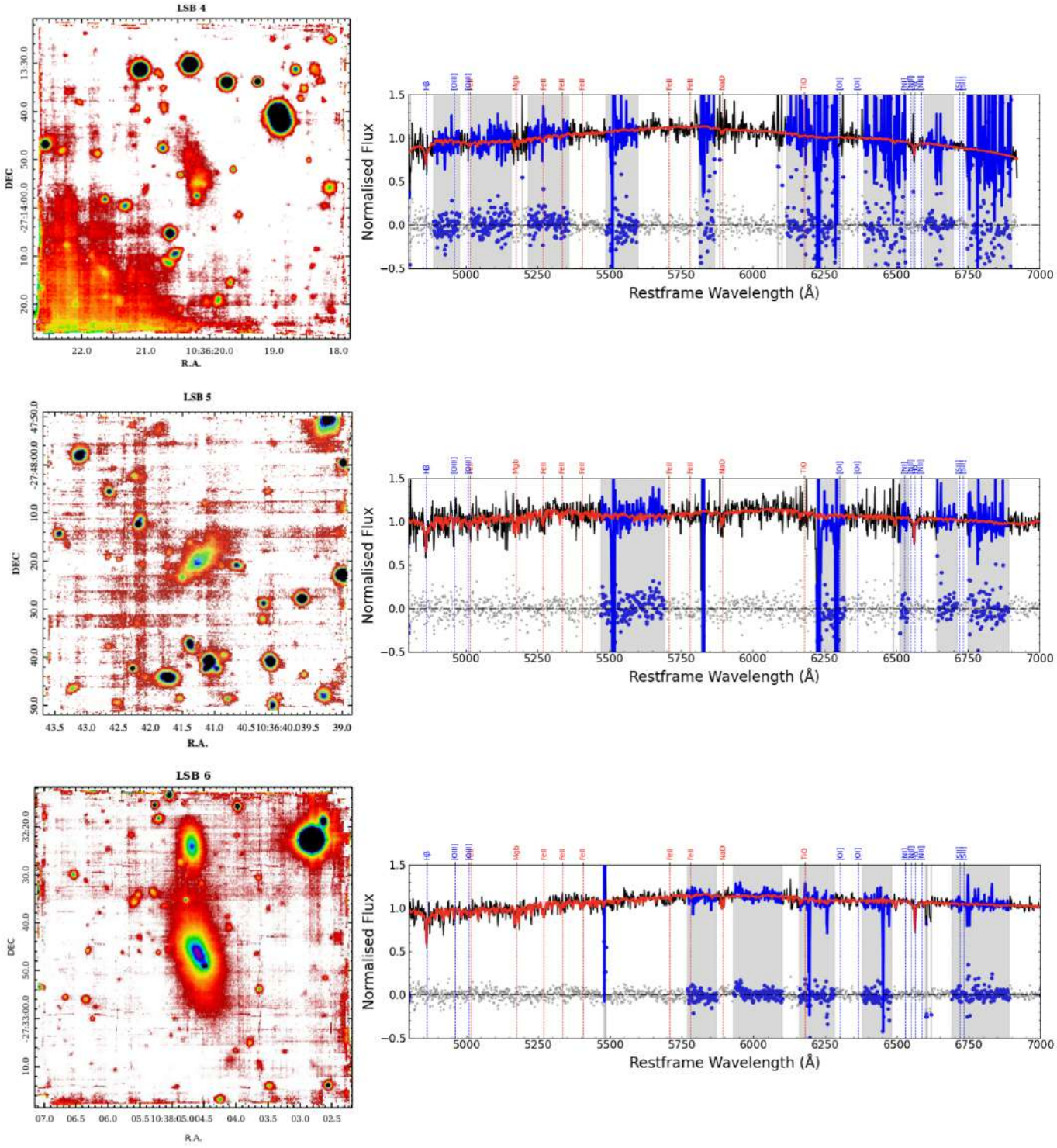

Fig. D.6. Same as Fig. D.1, but for LSB4, LSB5, and LSB6.

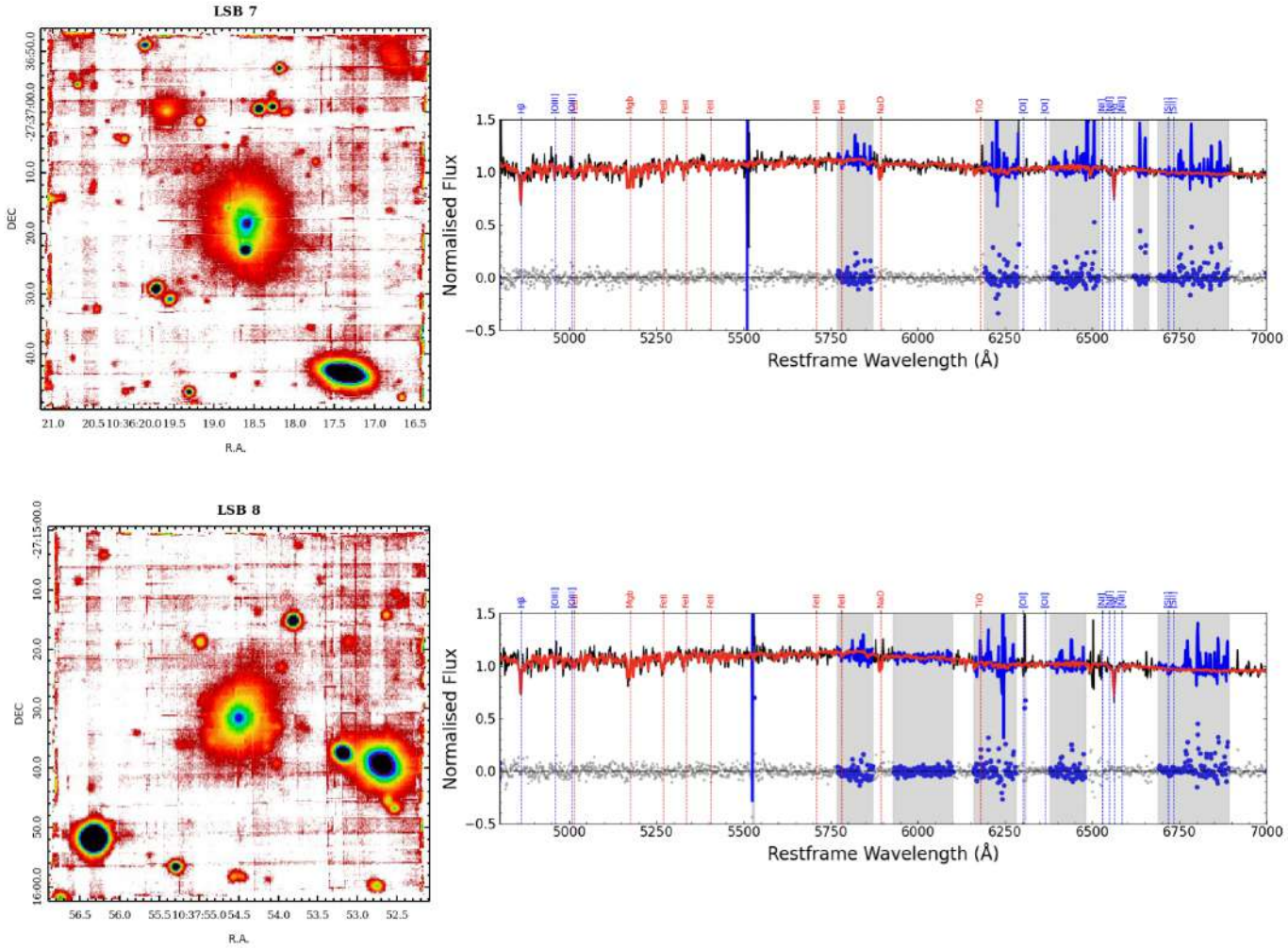

Fig. D.7. Same as Fig. D.1, but for LSB7 and LSB8.